

Linear stability analysis of detonations via numerical computation and dynamic mode decomposition

Dmitry I. Kabanov
*King Abdullah University of Science and Technology
Thuwal, Saudi Arabia*

Aslan R. Kasimov*
*P.N. Lebedev Physical Institute
Russian Academy of Sciences
Moscow, Russia*

(Dated:)

We introduce a new method to investigate linear stability of gaseous detonations that is based on an accurate shock-fitting numerical integration of the linearized reactive Euler equations with a subsequent analysis of the computed solution via the dynamic mode decomposition. The method is applied to the detonation models based on both the standard one-step Arrhenius kinetics and two-step exothermic-endothermic reaction kinetics. Stability spectra for all cases are computed and analyzed. The new approach is shown to be a viable alternative to the traditional normal-mode analysis used in detonation theory.

arXiv:1712.03276v1 [physics.flu-dyn] 8 Dec 2017

* kasimov@lpi.ru

I. INTRODUCTION

Shock waves arise in great many areas in physics: compressible gas dynamics, shallow-water flows, astrophysics, cosmology, quantum fluids, and many others. They are often accompanied by time-dependent dynamic phenomena related to instability of associated steady-state solutions. Such instability may be caused by interactions between the flow, geometry (boundaries, including the shock wave itself), and physical and chemical processes taking place in the flowing matter (such as magnetic field effects, chemical reactions, gravitation, quantum effects, and others) [7, 16–20, 22, 23, 34, 35, 40, 46, 60, 61].

Theoretical analysis of linear stability is usually based on the normal-mode method whereby the underlying governing system of partial differential equations is linearized, and the solution is represented as a certain mode, the form of which depends on the geometry of the problem. The mode is typically exponential in time as well as in those spatial directions in which the steady state is uniform [14]. In many interesting problems however, at least part of the steady-state structure is not uniform spatially, and as a result the modal problem becomes significantly more complicated. One typically must resort then to a numerical solution of the associated system of ordinary differential equations (ODEs) for the perturbation amplitudes. Finding an accurate and robust algorithm for such numerical solution can be challenging [14, 52]. For example, in a detonation problem considered in the present work, the challenge stems from the complexity of reaction rate equations that combined with the fluid equations, produce a system of ODEs that can be stiff and/or singular. As a result, performing accurate calculations of spectral properties becomes quite difficult [6, 27, 31, 42, 55, 58, 65, 71, 72].

Our goal in this paper is to introduce a new method for the calculation of linear stability properties of shock waves and detonations. The method consists of a direct numerical solution of a linearized system of governing equations with a subsequent modal analysis of the computed results for the presence of stable and unstable modes. One of the novelties of our technique is that growth rates and frequencies of the modes are extracted from the numerically computed time series with the implementation of the dynamic mode decomposition (DMD) [12, 29, 50].

The DMD is a powerful method to extract spectral information from complex data coming from numerical or experimental studies of various systems. It was introduced into analysis of fluid flows in [50, 54]. Importantly, even though the DMD has originated and found its most extensive use in fluid mechanics, the method is essentially model independent as it deals directly with data, irrespective of their origin. As such, it is of much interest in problems that involve large amounts of data, and for which there is a need to extract some global characteristic features. One can find the basic introduction to DMD as well as the discussion of many of its modern applications in [38]. The latter begin with fluid mechanics, but extend to numerous other fields involving “big data”: atmospheric science, image processing, epidemiology, neuroscience, financial markets and others. The problem of understanding data is especially acute when there is no known model that generates the data, for example, in the financial market or in neuroscience. In contrast, in fluid mechanics the data are governed by the Navier-Stokes or Euler equations, which are relatively well established.

Some of the recent developments of the method and its various applications can be found in [2, 4, 9, 11, 12, 29, 44, 45, 48, 51, 53, 62, 64, 67, 70]. There are interesting and deep mathematical roots of the method in the dynamical systems theory in connection with the so-called Koopman operator [36, 44, 49], which is an infinite-dimensional linear operator that represents a given finite-dimensional but nonlinear operator. Koopman theory, which is at the heart of DMD, can also be applied to analysis of various partial differential equations (PDEs) and ODEs [3, 39]. A modification of DMD was recently used to characterize chaotic systems [10]. In [68], the authors generalized DMD to optimal mode decomposition and showed that for noise-free linear systems, DMD correctly identifies system eigenvalues and hence is analogous to normal-mode analysis. Tu with co-authors in [64] gave a relatively simple description of the algorithm and showed that input data for DMD do not have to be sequential time series with a uniform time step between data snapshots. They also pointed out that snapshots must be sufficiently “rich” for the DMD to extract dynamic modes correctly. In [29], a sparsity-promoting version of DMD algorithm is proposed to achieve a balance between the quality of the extracted dynamics and the number of modes required to represent the dynamics. Several researchers considered sensitivity of DMD to the noise in input data. Duke with co-authors [15] considered synthetic wave shapes and carried out a detailed study of errors in growth rates and frequencies under varying parameters. The paper [5] demonstrated that output DMD eigenvalues are damped in the presence of noise, while [12] proposed four modifications for the DMD algorithm that alleviate noise effect. In [37, 70], criteria for choosing the rank of a low-order approximation are proposed, with [37] suggesting to determine relevant modes through its time-dependent amplitude, while [70] proposing to choose mode eigenfunctions on the basis of how good they approximate the corresponding Koopman operator eigenfunctions.

One can find applications of DMD in combustion problems as well. For example, the authors of [43] used DMD to investigate the dynamics of multidimensional detonations by analyzing the flow structures computed from the reactive compressible Navier-Stokes equations. We note that the analysis [43] was concerned with full nonlinear dynamics. In contrast, in this paper we investigate linear stability of one-dimensional reactive Euler equations. Thus our system is less general, however we provide more detailed and extensive analysis of the dynamics of the chosen model. In [47], DMD is applied to experimental study of combustion instability by stacking different flow observables (pressure, velocity, etc.).

In this work, we solve the linearized reactive Euler equations using a high-order space and time integration algorithm that is based on the shock fitting to avoid numerical shock-capturing errors [25, 26, 32, 63]. Using the new method, we calculate stability spectra and neutral boundaries for the problem and compare them with prior results found by the method of normal modes [42, 55, 58]. The computations are carried out for the standard one-step Arrhenius heat release and also for a two-step heat release with one exothermic and one endothermic reactions (the so-called ‘‘pathological detonation’’ [21, 56]).

For the standard one-step chemistry, we find complete agreement with the previously published results. For the two-step chemistry of the type $A \rightarrow B \rightarrow C$ where the first reaction is exothermic and the second is endothermic, we analyze both types (subsonic-supersonic and subsonic-subsonic) of the steady-state solutions that exist. For the subsonic-supersonic steady state, we qualitatively compare our result with the results of Sharpe [57] and again good agreement is found. Additionally, we calculate the stability of the subsonic-subsonic steady state and show that the eigenfunctions of the two steady-state solutions are the same between the shock and the sonic point, even though they are different downstream. Perhaps more importantly, our method of solution of the linear stability problem is essentially at the same level of complexity as that for the single-step chemistry case. In contrast, the method in [57] requires an intricate asymptotic analysis of perturbations in the neighborhood of the sonic locus such that an unbounded component of the solution can be identified and discarded. Imposing such a boundedness condition is generally the least understood and most difficult part of normal-mode stability analysis of detonations. The methodology proposed in the present work aims at circumventing this difficulty albeit at the expense of more extensive numerical calculations.

The remainder of the paper is organized as follows. In Section II, we introduce the governing system of reactive Euler equations. In Section III, we present the algorithms for the numerical integration of the linearized governing equations and for the processing of the generated time series of the shock velocity. In Section IV, calculations of instability of detonations with various rate functions are presented. In Section V, we discuss the results and possible extensions of the ideas presented in this work.

II. REACTIVE EULER EQUATIONS

Our analysis of detonation stability is based on the one-dimensional reactive Euler equations for a perfect gas that has a constant ratio of specific heats and reacts following either a single-step Arrhenius law or a two-step mechanism of the type $A \rightarrow B \rightarrow C$. The steady traveling-wave solutions for these two cases are investigated for linear stability by means of direct numerical integration of the linearized Euler equations with a subsequent analysis of the resultant time series of the shock speed using the DMD algorithm. In this section, we introduce the governing equations, their steady-state solutions and linearization about the steady state.

A. One-step Arrhenius kinetics

First, we present the governing equations for the case of one-step irreversible reaction



The progress of this reaction is followed by a variable λ such that the mass fraction of A is $1 - \lambda$ and that of B is λ .

The wave is assumed to propagate from left to right with speed D , and in the reference frame attached to the lead shock, the governing equations are written as [32]:

$$\rho_t + (\rho(u - D))_x = 0, \quad (2)$$

$$(\rho u)_t + (\rho u(u - D) + p)_x = 0, \quad (3)$$

$$(\rho e)_t + (\rho(u - D)e + pu)_x = 0, \quad (4)$$

$$(\rho \lambda)_t + (\rho(u - D)\lambda)_x = \rho \omega. \quad (5)$$

where ρ , u , p , e , ω are density, flow velocity, pressure, total specific energy, and reaction rate, respectively. The specific energy is $e = e_i + u^2/2$ with constitutive relations of a calorically perfect gas:

$$e_i = \frac{pv}{\gamma - 1} - Q\lambda, \quad pv = RT, \quad (6)$$

where γ is the polytropic index, $v = 1/\rho$ specific volume, Q chemical heat release, R the universal gas constant, T temperature. The reaction rate is taken here to follow simple-depletion Arrhenius law:

$$\omega = k(1 - \lambda) \exp\left(-\frac{E\rho}{p}\right), \quad (7)$$

where k is rate constant and E the activation energy.

The numerical solution of the governing equations (2–5) in the shock-attached frame requires an evolution equation for D which is present explicitly in the equations. For this purpose, we use the equation derived in [63] by specializing it to one dimension:

$$\frac{dM}{dt} = s, \quad (8)$$

where $M = -\rho_a D$ is the normal mass flux into the shock, ρ_a is the upstream density, and

$$s = \frac{1}{A_0} (R_s - A_s), \quad A_0 = \frac{2}{\gamma + 1} M v_a \left(3 + \frac{\gamma p_a \rho_a}{M^2} \right), \quad (9)$$

$$R_s = Q(\gamma - 1) \rho_s \omega_s, \quad A_s = \rho_s (c_s^2 - U_s^2) u_x|_s, \quad (10)$$

where $c = \sqrt{\gamma p / \rho}$ is the sound speed, $U = u - D$ is the flow velocity in the shock-attached frame, subscript “s” denotes the shock state and subscript “a” the ambient (upstream) state. Note that in (9–10) everything depends on the shock state through the Rankine-Hugoniot conditions except for the velocity gradient $u_x|_s$ at the shock, which must be determined numerically by solving for the flow downstream.

The Rankine–Hugoniot conditions at $x = 0$ give all the state variables in terms of the mass flux (or, equivalently, the shock speed):

$$p_s = -\frac{\gamma - 1}{\gamma + 1} p_a + \frac{2v_a}{\gamma + 1} M^2, \quad v_s = \frac{\gamma - 1}{\gamma + 1} v_a + \frac{2}{\gamma + 1} \frac{\gamma p_a}{M^2}, \quad U_s = M v_s, \quad (11)$$

and $\lambda_s = 0$, $\rho_s = 1/v_s$.

Next, we introduce the vector of state variables $z = (\rho, u, p, \lambda)^T$ and linearize it as well as the shock speed as $z(x, t) = \bar{z}(x) + \epsilon z'(x, t)$, $D(t) = \bar{D} + \epsilon \psi'(t)$, with $0 < \epsilon \ll 1$, the bar denoting the steady-state, and the prime denoting the perturbation amplitudes. Upon linearization of the governing equations (2–5), we obtain

$$z'_t + A(\bar{z}) z'_x + B(\bar{z}) z' - \frac{d\bar{z}}{dx} \psi' = 0, \quad (12)$$

where

$$A = \begin{bmatrix} \bar{U} & \bar{p} & 0 & 0 \\ 0 & \bar{U} & 1/\bar{\rho} & 0 \\ 0 & \gamma \bar{p} & \bar{U} & 0 \\ 0 & 0 & 0 & \bar{U} \end{bmatrix}, \quad B = \begin{bmatrix} \frac{d\bar{u}}{dx} & \frac{d\bar{p}}{dx} & 0 & 0 \\ -\frac{1}{\bar{\rho}^2} \frac{d\bar{p}}{dx} & \frac{d\bar{u}}{dx} & 0 & 0 \\ C(\bar{\rho}\bar{\omega}_\rho + \bar{\omega}) & \frac{d\bar{p}}{dx} & \gamma \frac{d\bar{u}}{dx} + C\bar{\rho}\bar{\omega}_p & C\bar{\rho}\bar{\omega}_\lambda \\ -\bar{\omega}_\rho & \frac{d\bar{\lambda}}{dx} & -\bar{\omega}_p & -\bar{\omega}_\lambda \end{bmatrix}, \quad (13)$$

$C = -(\gamma - 1)Q$, and subscripts ρ , p and λ denote partial derivatives.

The linearization of the Rankine–Hugoniot conditions and the shock-evolution equation yields:

$$p'_s = \frac{4v_a \bar{M}}{\gamma + 1} M', \quad v'_s = -\frac{4\gamma p_a}{(\gamma + 1) \bar{M}^3} M', \quad U'_s = \bar{M} v'_s + \bar{v}_s M', \quad \rho'_s = -\frac{v'_s}{\bar{v}_s^2}, \quad \lambda'_s = 0, \quad (14)$$

$$\frac{dM'}{dt} = s', \quad (15)$$

where

$$s' = \frac{1}{A_0} (R'_s - A'_s) - \frac{A'_0}{A_0^2} (\bar{R}_s - \bar{A}_s), \quad (16)$$

$$A'_0 = \frac{2}{\gamma + 1} \frac{3v_a \bar{M}^2 - \gamma p_a}{\bar{M}^2} M', \quad R'_s = Q(\gamma - 1) \left[(\bar{\rho}\bar{\omega}_\rho + \bar{\omega}) \rho' + \bar{\rho}\bar{\omega}_p p' \right] \Big|_s, \quad (17)$$

$$A'_s = \left[\rho \frac{d\bar{u}}{dx} (\gamma (\bar{p}v' + \bar{v}p') - 2\bar{U}U') + (\bar{c}^2 - \bar{U}^2) \frac{d\bar{u}}{dx} \rho' + \bar{\rho} (\bar{c}^2 - \bar{U}^2) u'_x \right] \Big|_s \quad (18)$$

with all the spatially-dependent quantities on the right-hand sides of R'_s and A'_s evaluated at the shock.

The base steady-state traveling wave is the ZND solution (after Zel'dovich [69], von Neumann [66] and Döring [13]) given in terms of $\bar{\lambda}$ and \bar{D} by [63]:

$$\bar{v} = \frac{\gamma}{\gamma + 1} \frac{\bar{P}}{\bar{M}^2} (1 - \delta), \quad \bar{p} = \bar{P} - \bar{M}^2 \bar{v}, \quad \bar{U} = \bar{M} \bar{v}, \quad (19)$$

where

$$\delta = \sqrt{1 - \frac{h \bar{M}^2}{\bar{P}^2} (\bar{H} + Q \bar{\lambda})}, \quad h = \frac{2(\gamma^2 - 1)}{\gamma^2}, \quad (20)$$

and $\bar{P} = p_a + \rho_a \bar{D}^2$, $\bar{H} = e_a + p_a / \rho_a + \bar{D}^2 / 2$. To obtain the solution in terms of x , the steady-state rate equation

$$\frac{d\bar{\lambda}}{dx} = \frac{\bar{\omega}}{\bar{U}} \quad (21)$$

is integrated starting at the shock with the initial condition $\bar{\lambda}_s = 0$ and auxiliary relations (19) and (20).

For self-sustained detonations with the Arrhenius kinetics (7) the flow becomes sonic relative to the shock at the end of the reaction zone $\lambda = 1$, which is located at $x \rightarrow -\infty$. Then $\delta = 0$ at $\lambda = 1$ [30, 33], and it follows that $\bar{D} = D_{CJ}$ where

$$D_{CJ} = \sqrt{c_a^2 + q} + \sqrt{q}, \quad q = \frac{(\gamma^2 - 1)Q}{2}, \quad c_a^2 = \frac{\gamma p_a}{\rho_a}. \quad (22)$$

The pre-exponential factor k defines the length scale and is chosen following the standard practice such that the half-reaction length is unity:

$$k = \int_0^{1/2} \frac{\bar{U}}{(1 - \bar{\lambda}) \exp(-E \bar{\rho} / \bar{p})} d\bar{\lambda}. \quad (23)$$

B. Two consecutive reactions

Now consider a simple example of a multi-step chemistry that consists of two consecutive reactions:



where the first reaction is exothermic and the second endothermic. This is often referred to as the case of a ‘‘pathological’’ detonation [21]. The unfortunate name comes from the fact that the detonation in this case propagates faster than expected, the expectation based on the (wrong) thinking that it is the overall heat release that controls the detonation speed. In reality, it is not the overall but rather the maximum heat release—which is larger—that controls the wave speed. This should become clear from the analysis of the steady-state structure that follows.

Let the reactions have rate constants k_1 and k_2 , heat releases $Q_1 > 0$ and $Q_2 < 0$, and activation energies, E_1 and E_2 , for the first ($A \rightarrow B$), and second, ($B \rightarrow C$), reactions, respectively. Then, if X_A , X_B , and X_C denote the mass fractions of the species, the kinetic equations for the reactions are

$$\dot{X}_A = -k_1 X_A e^{-E_1/RT}, \quad (25)$$

$$\dot{X}_B = k_1 X_A e^{-E_1/RT} - k_2 X_B e^{-E_2/RT}, \quad (26)$$

$$\dot{X}_C = k_2 X_B e^{-E_2/RT}. \quad (27)$$

Adding these equations and noting that initially $X_A = 1$, $X_B = X_C = 0$, we find that $X_A + X_B + X_C = 1$. We introduce the reaction progress variables for each reaction as $\lambda_1 = 1 - X_A$ and $\lambda_2 = X_C$ with λ_1 and λ_2 varying from 0 at the shock to 1 at the end of the reaction. Then we obtain the following rate equations

$$(\rho \lambda_1)_t + (\rho(u - D) \lambda_1)_x = \rho \omega_1, \quad (28)$$

$$(\rho \lambda_2)_t + (\rho(u - D) \lambda_2)_x = \rho \omega_2, \quad (29)$$

with $\omega_1 = k_1 (1 - \lambda_1) e^{-E_1/RT}$ and $\omega_2 = k_2 (\lambda_1 - \lambda_2) e^{-E_2/RT}$. These equations replace the rate equation (5). The specific internal energy becomes $e_i = p\nu/(\gamma - 1) - (Q_1\lambda_1 + Q_2\lambda_2)$. The steady-state formulas retain their form with $Q\lambda$ replaced by $Q_1\lambda_1 + Q_2\lambda_2$. In particular,

$$\delta = \sqrt{1 - \frac{h\bar{M}^2}{\bar{P}^2} (H + Q_1\bar{\lambda}_1 + Q_2\bar{\lambda}_2)}. \quad (30)$$

Recall that $\delta = 0$ when the flow becomes sonic relative to the shock [30]. Then, for δ to have a derivative that is everywhere bounded we require that

$$Q_1 \frac{d\bar{\lambda}_1}{dx} + Q_2 \frac{d\bar{\lambda}_2}{dx} = 0 \text{ whenever } \delta = 0. \quad (31)$$

This means that the heat release has a maximum at the sonic point. The solution of $\delta = 0$ yields the same result for \bar{D} as before, i.e.,

$$\bar{D} = \sqrt{c_a^2 + \frac{\gamma^2 - 1}{2} (Q_1\bar{\lambda}_1^* + Q_2\bar{\lambda}_2^*)} + \sqrt{\frac{\gamma^2 - 1}{2} (Q_1\bar{\lambda}_1^* + Q_2\bar{\lambda}_2^*)} \quad (32)$$

with star denoting the sonic locus. The first of the conditions (31) (known as the thermicity condition [21]) can be written using the steady-state rate equations

$$\bar{U} \frac{d\bar{\lambda}_1}{dx} = \bar{\omega}_1, \quad \bar{U} \frac{d\bar{\lambda}_2}{dx} = \bar{\omega}_2 \quad (33)$$

as

$$Q_1\bar{\omega}_1^* + Q_2\bar{\omega}_2^* = 0. \quad (34)$$

It follows from this equation that

$$\bar{\lambda}_2^* = \bar{\lambda}_1^* + \frac{k_1 Q_1}{k_2 Q_2} (1 - \bar{\lambda}_1^*) \exp\left(-\frac{E_1 - E_2}{R\bar{T}^*}\right), \quad (35)$$

where \bar{T}^* is some complicated function of $\bar{\lambda}_1^*$, $\bar{\lambda}_2^*$ and \bar{D} that can be found from the steady-state relations.

Generally, the sonic state and the detonation speed are calculated as follows. For a chosen \bar{D} , one solves (33) starting from the shock to the sonic point, x_* , where the sonic conditions (32) and (34) must be satisfied. For arbitrary \bar{D} , these conditions will not be satisfied, and instead the steady-state solution will blow up. But for special \bar{D} (one or more), the solution will pass continuously (however, not necessarily smoothly) through x_* to the equilibrium state at $x \rightarrow -\infty$. This is a general numerical procedure that can be followed to determine the detonation speed \bar{D} .

We however restrict our attention in this work to the case $E_1 = E_2$ which allows for a more explicit analytical calculation that will facilitate both the theory and numerical computations that follow. Expression (35) simplifies then to

$$\bar{\lambda}_2^* = \bar{\lambda}_1^* + \frac{k_1 Q_1}{k_2 Q_2} (1 - \bar{\lambda}_1^*). \quad (36)$$

Upon division of the second equation in (33) by the first, we obtain

$$\frac{d\bar{\lambda}_2}{d\bar{\lambda}_1} = k_r \frac{\bar{\lambda}_1 - \bar{\lambda}_2}{1 - \bar{\lambda}_1}, \quad (37)$$

where $k_r = k_2/k_1$. The linear equation (37) can be integrated to yield

$$\bar{\lambda}_2 = \begin{cases} 1 - \frac{(1-\bar{\lambda}_1)^{k_r} - k_r(1-\bar{\lambda}_1)}{1-k_r}, & k_r \neq 0, \\ 1 - (1 - \bar{\lambda}_1) (1 - \ln(1 - \bar{\lambda}_1)), & k_r = 1. \end{cases}$$

Thus, to find $\bar{\lambda}_1^*$, we need to substitute one of these expressions for $\bar{\lambda}_2$ into (36) and then solve the resultant nonlinear equation for $\bar{\lambda}_1^*$, which requires a numerical iterative procedure. If we further restrict the case to $k_r = 1$, we find explicitly that

$$(1 - \bar{\lambda}_1^*) \left[\ln(1 - \bar{\lambda}_1^*) - \frac{Q_1}{Q_2} \right] = 0, \quad (38)$$

from which it follows that either $\bar{\lambda}_1^* = \bar{\lambda}_1^e = 1$, which is the equilibrium state, or

$$\bar{\lambda}_1^* = 1 - \exp(Q_1/Q_2), \quad (39)$$

which is the embedded sonic state.

For the equilibrium case, $\bar{\lambda}_1^e = \bar{\lambda}_2^e = 1$, the wave speed can be found from $\delta_e = 0$, and it is the same as given in (22) with $Q = Q_1 + Q_2$. This is sometimes called an ‘‘equilibrium CJ solution’’. We emphasize however that even though formally we can calculate this velocity, in reality the governing equations have no solution at this speed, and therefore it makes no sense to talk about ‘‘equilibrium CJ solution’’. The reason for the lack of solution can be seen from (30). The expression $Q_1\bar{\lambda}_1 + Q_2\bar{\lambda}_2$ goes from 0 at the shock to $Q_1 + Q_2$ at equilibrium, but along the way, it has a maximum at the embedded sonic state. Therefore, if $\delta = 0$ at $\bar{\lambda}_1 = \bar{\lambda}_2 = 1$, then the expression under the square root in (30) would have to take on negative values in some part of the reaction zone, which is of course impossible. Thus, we must exclude the ‘‘equilibrium CJ solution’’ from consideration.

The second case gives an embedded sonic locus. The flow is divided then by the sonic point into two parts. Between the shock and the sonic point, the flow is always subsonic relative to the shock. Between the sonic point and equilibrium point, the flow can be either subsonic or supersonic: flow is supersonic if expression (30) is used as is, while subsonic if the sign of the right-hand side of (30) is changed to negative [30]. Thus we obtain two steady-state solutions with the embedded sonic locus. Stability of both will be investigated below.

The linearized perturbation system is the same as before, but with $z = (\rho, u, p, \lambda_1, \lambda_2)^T$ and with the following new matrices of coefficients (with $C_i = -(\gamma - 1)Q_i$ and $i = 1, 2$):

$$A = \begin{bmatrix} \bar{U} & \bar{\rho} & 0 & 0 & 0 \\ 0 & \bar{U} & 1/\bar{\rho} & 0 & 0 \\ 0 & \gamma\bar{p} & \bar{U} & 0 & 0 \\ 0 & 0 & 0 & \bar{U} & 0 \\ 0 & 0 & 0 & 0 & \bar{U} \end{bmatrix}, \quad B = \begin{bmatrix} \frac{d\bar{u}}{dx} & \frac{d\bar{p}}{dx} & 0 & 0 & 0 \\ -\frac{1}{\bar{\rho}^2} \frac{d\bar{p}}{dx} & \frac{d\bar{u}}{dx} & 0 & 0 & 0 \\ \sum_i C_i(\bar{\rho}\bar{\omega}_{i\rho} + \bar{\omega}_i) \frac{d\bar{p}}{dx} & \gamma \frac{d\bar{u}}{dx} + \bar{\rho} \sum_i C_i \bar{\omega}_{i\rho} & \bar{\rho} \sum_i C_i \bar{\omega}_{i\lambda_1} & \bar{\rho} \sum_i C_i \bar{\omega}_{i\lambda_2} & \\ -\bar{\omega}_{1\rho} & \frac{d\bar{\lambda}_1}{dx} & -\bar{\omega}_{1\rho} & -\bar{\omega}_{1\lambda_1} & -\bar{\omega}_{1\lambda_2} \\ -\bar{\omega}_{2\rho} & \frac{d\bar{\lambda}_2}{dx} & -\bar{\omega}_{2\rho} & -\bar{\omega}_{2\lambda_1} & -\bar{\omega}_{2\lambda_2} \end{bmatrix}. \quad (40)$$

For the shock evolution equation we obtain

$$\bar{R}_s = (\gamma - 1)\rho_s \sum_i Q_i \bar{\omega}_{is}, \quad (41)$$

$$R'_s = (\gamma - 1) \sum_i Q_i [(\bar{\rho}\bar{\omega}_{i\rho} + \bar{\omega}_i) \rho' + \bar{\rho}\bar{\omega}_{i\rho} p']|_s. \quad (42)$$

All the other expressions remain as before.

The equations are rescaled using the so-called Erpenbeck scales such that $\rho_a = p_a = 1$, velocity is scaled by $\sqrt{p_a/\rho_a}$, spatial scale is that of the half-reaction length. With these scales, equations keep their form. Activation energy and heat release are rescaled by the ambient temperature multiplied by R .

III. THE NUMERICAL SOLUTION PROCEDURE

To determine stability properties of self-sustained detonations for any particular set of physical parameters Q , E , and γ , we solve an initial boundary value problem for (12–15) numerically to see if its solution grows or decays in time. In each simulation, after an initialization stage consisting of grid partitioning and the evaluation of ZND quantities on the grid, the linear system is integrated in time with simultaneous recording of the time series of the perturbation of detonation velocity, ψ' , and then the time series are post-processed using DMD to extract a stability spectrum. Each of these stages is described in detail below.

With the rate function (7), the reaction zone is formally infinite. For numerical simulations, this length must be truncated to some finite value \mathcal{L} . We determine \mathcal{L} by the closeness of the reaction progress variable of the ZND solution $\bar{\lambda}$ to unity at the end of the reaction zone as measured by some tolerance tol_λ . Once tol_λ is specified, we compute \mathcal{L} using

$$\mathcal{L} = \lceil I \rceil \text{ with } I = \int_0^{1-\text{tol}_\lambda} \frac{\bar{U}}{k(1-\bar{\lambda}) \exp(-\bar{\rho}E/\bar{p})} d\bar{\lambda}, \quad (43)$$

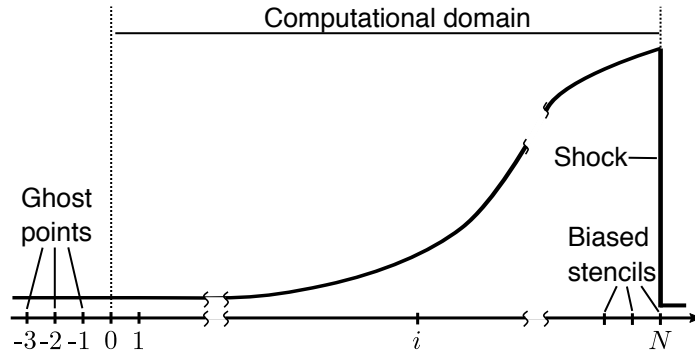


Figure 1. Schematics of the numerical grid.

where k is computed from (23). The computational domain is then discretized using a uniform grid $\{x_i\}$, $i = 0, \dots, N$ with $N = N_{1/2}\mathcal{L}$; $x_0 = -\mathcal{L}$ and $x_N = 0$ being left and right boundary points, respectively. Here $N_{1/2}$ denotes the number of grid points per unit length (to remind, the unit length is the distance from the shock to the point where $\lambda = 1/2$, hence the index $1/2$). The spatial step of the grid is $\Delta x = 1/N_{1/2}$. Schematically, the grid is shown in Figure 1.

The steady-state ZND profiles are computed on the grid using (19-21) via the numerical integrator VODE [8] with the BDF method of fifth order with absolute and relative tolerances set to 10^{-15} . Also, all other ZND quantities that enter matrices $A(\bar{z})$ and $B(\bar{z})$ in (13) are computed.

A. Integration of the linearized system

After the initialization stage, an unsteady solution of the linearized system is computed by the method of lines. At each time step, the spatial derivatives are first approximated on the numerical grid thereby converting the system of PDEs (12-15) to a system of ODEs:

$$\frac{dz'_i}{dt} = -\widehat{L}(\bar{z}, z'), \quad i = 1, \dots, N-1, \quad (44)$$

$$\frac{dM'}{dt} = \widehat{s}(\bar{z}, z'), \quad (45)$$

where $\widehat{L}(\bar{z}, z', z'_x)$ and $\widehat{s}(\bar{z}, z')$ are approximations of $L(\bar{z}, z', z'_x) = A(\bar{z})z'_x + B(\bar{z})z' - \frac{d\bar{z}}{dx}\psi'$ from (12) and $s(\bar{z}, z', z'_x)$ from (15), respectively. In these expressions, the spatial derivatives are evaluated using finite-difference formulas as given below, and then the system is evolved in time over one time step Δt .

The spatial derivatives are calculated in the following four steps.

1. Approximation at points $i = 0, \dots, N-3$. We compute left- and right-biased approximations of z'_x based on the upwind method of fifth order:

$$z_x^-|_i = \frac{-2z_{i-3} + 15z_{i-2} - 60z_{i-1} + 20z_i + 30z_{i+1} - 3z_{i+2}}{60\Delta x}, \quad (46)$$

$$z_x^+|_i = \frac{3z_{i-2} - 30z_{i-1} - 20z_i + 60z_{i+1} - 15z_{i+2} + 2z_{i+3}}{60\Delta x}, \quad (47)$$

where subscripts “-” and “+” denote left- and right-biased approximations, respectively.

2. Approximation at $i = N-2$. At this grid point, the Taylor expansion gives a fifth-order formula

$$z_x'|_{N-2} = \frac{-2z_{N-5} + 15z_{N-4} - 60z_{N-3} + 20z_{N-2} + 30z_{N-1} - 3z_N}{60\Delta x}. \quad (48)$$

3. Approximation at $i = N-1$. At this point, spatial derivatives are approximated using the fourth-order formula

$$z_x'|_{N-1} = \frac{-z_{N-4} + 6z_{N-3} - 18z_{N-2} + 10z_{N-1} + 3z_N}{12\Delta x}. \quad (49)$$

4. Approximation at $i = N$. At this point, only u'_x must be approximated because it appears in the shock-evolution equation (45). The approximation formula is

$$u'_x|_N = \frac{-12u_{N-5} + 75u_{N-4} - 200u_{N-3} + 300u_{N-2} - 300u_{N-1} + 137u_N}{60\Delta x}. \quad (50)$$

Expressions (48)–(50) were first used for detonation simulations in [26] in a shock-fitting algorithm.

Once the spatial derivatives are approximated, \widehat{L} is found using the global Lax–Friedrichs flux:

$$\widehat{L}(\bar{z}, z') = L\left(\bar{z}, z', \frac{z_x'^- + z_x'^+}{2}\right) - \alpha \frac{z_x'^+ - z_x'^-}{2}, \quad (51)$$

where $z_x'^- = z_x'^+ = z_x'$ for grid points $i = \{N - 2, N - 1, N\}$, α is the largest eigenvalue of $A(\bar{z})$ over the numerical grid,

$$\alpha = \max_{i=0, \dots, N} \{\bar{u} - \bar{c}, \bar{u}, \bar{u} + \bar{c}\}|_{x=x_i}. \quad (52)$$

We found that a simple evaluation of L was not enough to guarantee numerical stability of simulations, hence the use of the Lax–Friedrichs flux in (51). After evaluation of L , $\widehat{s}(\bar{z}, z')$ is found using the approximation of $u_x|_s$ given by (50).

Once $\widehat{L}(\bar{z}, z')$ and $\widehat{s}(\bar{z}, z')$ are evaluated on the whole grid, system (44–45) is evolved in time using the adaptive-step time integrator DOPRI5 [25], which is an embedded pair of explicit Runge–Kutta methods of orders 5 and 4 used to estimate a local error. We set both absolute and relative tolerances of the time integrator to 10^{-14} .

Simulation proceeds to the final time T_f , where typically $T_f = 10$ is used. While computing the solution, we record the time series of the perturbation of detonation velocity $\psi'(t)$ at uniform time intervals $\Delta t = 0.005$. When simulation reaches T_f , the solver computes the ratio of L_2 -norms of the time series for $T_f/2 \leq t \leq T_f$ and $0 \leq t \leq T_f/2$, and if this ratio is smaller than three, then T_f is increased to 100, as we found it necessary to record longer time series when the flow is not sufficiently unstable. The analysis of the resulting time series of the perturbation of detonation velocity allows us to extract growth rates and frequencies of unstable modes by a post-processing method described below in Subsection III B.

We also need to provide initial conditions for z' and M' . First, the perturbation of the detonation velocity by a small value $A_0 = 10^{-10}$ is specified. Then, the initial value of M' is computed using $M' = -\rho_a A_0$. The Rankine–Hugoniot conditions are then used to find ρ'_s, u'_s, p'_s from M' . Subsequently, initial conditions for perturbations over the whole grid are computed using

$$\rho'_0(x) = \frac{\rho'_s}{\bar{\rho}_s} \bar{\rho}(x), \quad u'_0(x) = \frac{u'_s}{\bar{u}_s} \bar{u}(x), \quad p'_0(x) = \frac{p'_s}{\bar{p}_s} \bar{p}(x), \quad \lambda'_0(x) = A_0 \bar{\lambda}(x). \quad (53)$$

As can be seen from these formulas, the initial conditions for perturbations are specified as a multiple of the ZND solution. We found that such an initial condition minimizes the transient behavior in the time series of ψ' at early times. The beginning of the time series is cut off before the post-processing in order to eliminate the initial numerical transients from the signal.

Whenever the time integrator evaluates the right-hand side of system (44–45), boundary conditions are imposed as follows. At the shock (grid point $i = N$), boundary conditions are specified using (14). At the downstream end, no boundary condition should be specified for the system, however, boundary treatment is necessary for the finite-difference computations [41]. This is done by the zeroth-order extrapolation:

$$z'_i = z'_0 \text{ for } i \in \{-3, -2, -1\},$$

where negative indices are used for the ghost grid points to the left of the computational domain. For the fifth-order upwind method (46–47) three ghost points are needed.

The algorithm was verified to be fifth order in space and time either by measuring the convergence rate to the steady-state solution (in stable cases) or by a self-convergence test (in unstable cases).

B. DMD analysis of the numerical results

In the postprocessing step, our goal is to extract growth rates and frequencies of unstable modes (discrete stability spectrum) from the time series of detonation velocity

$$\psi'(t) = [\psi'_0, \psi'_1, \dots, \psi'_n]^T, \quad (54)$$

where n is the index of the last time step and values ψ'_k are defined at times t_k , $k = 0, \dots, n$ such that $t_k - t_{k-1} = \Delta t = \text{const}$ for all $k = 1, \dots, n$.

To process such a time series, an efficient and robust algorithm is required such that the stability spectrum is computed as accurately as possible. The DMD algorithm [50] is at the heart of our postprocessing. We note however, that the DMD algorithm does not necessarily answer the question of what the rank of low-dimensional approximation should be. Hence, we need a way to determine the best approximation with the ultimate goal being to find all modes that can also be found by normal-mode analysis.

The remainder of this section proceeds as follows. First, for completeness, we present a brief generic description of the DMD algorithm. Then, we describe how we form input data for the DMD algorithm from the time series (54), and explain how we determine the best low-rank approximation. Finally, we apply the algorithm to synthetic data to assess its performance.

1. Description of the DMD algorithm

Suppose that we have a time series of the snapshots of the state of some dynamical system:

$$x = [x_0, \dots, x_n]^T, \quad (55)$$

where $x_i \in \mathbb{R}^m$ for all $i = 0, \dots, n$, and x_i being a snapshot of the system state. Assume also that snapshots are taken at uniform time intervals Δt . Our purpose is to find an eigendecomposition of a linear operator A such that

$$x_k = Ax_{k-1}$$

for all $k = 1, \dots, n$ at least in the least-squares sense. The eigenvalues of A contain the information on the growth/decay rates and frequencies of oscillations that, when combined, represent the time evolution of the dynamical system.

To proceed, we define matrices

$$X = [x_0, \dots, x_{n-1}]^T, \quad Y = [x_1, \dots, x_n]^T \quad (56)$$

such that $Y = AX$ and thus $A = YX^\dagger$, where X^\dagger is a Moore–Penrose pseudoinverse of X . Although the problem is formally solved now, we cannot just do the eigendecomposition of A because $A \in \mathbb{R}^{m \times m}$ with m generally being large. Instead, a low-rank approximation matrix \tilde{A} and its eigendecomposition are found. With given inputs (56), the DMD algorithm proceeds as follows:

1. Compute reduced singular value decomposition (SVD) of X :

$$X = U\Sigma V^T, \quad (57)$$

with matrices U and V having orthonormal columns and Σ being diagonal with singular values σ_i , $i = 1, \dots, \min(m, n)$, on the diagonal.

2. Truncate U , Σ , and V to rank r , which yields matrices U_r , Σ_r , and V_r . Truncation is necessary, for example, because all singular values σ_i in Σ with $i > r$ are due to the noise in matrix X .

3. Compute auxiliary matrix $\tilde{A} \in \mathbb{R}^{r \times r}$:

$$\tilde{A} = U_r^T A U_r = U_r^T Y X^\dagger U_r = U_r^T Y V_r \Sigma_r^{-1} U_r^T U_r = U_r^T Y V_r \Sigma_r^{-1}.$$

4. Find eigendecomposition of \tilde{A} :

$$\tilde{A}W = W\Lambda,$$

where $\Lambda = \text{diag}(\lambda_1, \dots, \lambda_r)$ is the matrix of eigenvalues, W the matrix of eigenvectors.

5. Find truncated eigendecomposition of A . All eigenvalues of \tilde{A} are the eigenvalues of A as well (the opposite is not necessarily true as $\tilde{A} \in \mathbb{R}^{r \times r}$ while $A \in \mathbb{R}^{m \times m}$ with $r \leq m$). Matrix of eigenvectors Φ of A can be found using

$$\Phi = Y V_r \Sigma_r^{-1} W \Lambda^{-1},$$

with Φ being a rectangular matrix containing exact DMD modes as was introduced in [64].

Knowing the eigenvalues Λ and eigenvectors Φ of A , we can reconstruct the time series (55):

$$\widehat{x}_k = Ax_{k-1} = A^k x_0 = \Phi \Lambda^k b, \quad (58)$$

where $b = \Phi^\dagger x_0$ is the vector of the initial amplitudes of DMD modes. Hence, DMD provides modes which are separated in terms of frequencies (that is, imaginary parts of λ_i).

To measure the quality of low-rank approximation, the relative error e_{DMD} and residual error e_{resid} are computed:

$$e_{\text{DMD}} = \frac{\|\widehat{x} - x\|_2}{\|x\|_2}, \quad e_{\text{resid}} = \|Y - \Phi \Lambda \Phi^\dagger X\|_2. \quad (59)$$

We also convert discrete-time eigenvalues λ_i that imply stability when they are inside the unit disc in \mathbb{C} to the continuous-time eigenvalues α_i that imply stability when they are in the left half-plane of \mathbb{C} as they are commonly used in normal-mode analysis. The conversion formula is

$$\alpha_i = \frac{\log(\lambda_i)}{\Delta t}, \quad i = 1, \dots, r.$$

2. Application of DMD to the time series of detonation velocity

The DMD as it was introduced in [50] assumes that each snapshot in a time series is a high-dimensional vector coming, for example, from a solution variable on a numerical grid at a given time step in simulations or from a large number of flow sensors in experiments. The time series of perturbation of detonation velocity ψ' (54) that we record during our simulations are one-dimensional, that is, $\psi'_k \in \mathbb{R}$, $k = 0, \dots, n$. As pointed out in [64, pp. 401–402], one-dimensional time series yields the matrix \tilde{A} which is 1×1 , therefore it has only one real eigenvalue, which can only capture an exponential growth or decay, but not oscillations. To overcome this rank-deficiency problem, we build an input Hankel matrix Z :

$$Z = \begin{bmatrix} \psi'_0 & \cdots & \psi'_{n-L} \\ \psi'_1 & \cdots & \psi'_{n-L+1} \\ \vdots & \vdots & \vdots \\ \psi'_{L-1} & \cdots & \psi'_n \end{bmatrix}, \quad (60)$$

which stacks time-shifted values of ψ' . This approach is commonly used in other methods of time-series analysis such as Singular Spectral Analysis [24]. Number L in (60) defines the upper bound on the number of modes that we can extract from the time series. In this paper, $L = 1000$ is used. Then, the input matrices X and Y (56) are built from Z by excluding the last and first columns of Z , respectively.

As time series of ψ' inevitably contains noise induced by truncation and rounding errors of the numerical computations, truncation of matrices U , Σ , and V from (57) with a target rank r will yield a matrix $\tilde{A} \in \mathbb{R}^{r \times r}$ whose eigenvalues are all physical only if r is known *a priori*. However, if the rank choice is done by a machine, there is always a possibility that the value of r will be larger than the rank of the ideal low-rank approximation, hence, the spurious eigenvalues will be present in the output of DMD (with even more severe consequences if, for example, instead of a complex-conjugate pair of eigenvalues only one real eigenvalue would be found). As we aim to apply DMD in Section IV for parametric studies of detonation stability, an algorithm is needed for choosing the target rank r automatically and as accurately as possible. The details of the algorithm that we use are provided below.

First, the beginning of the time series (54) must be cut off as it is necessary to exclude determining DMD modes from nonmodal behavior occurring due to the relaxation of the perturbation solution from volatile initial conditions (53) to a superposition of modes. This cutoff time depends on the length of the time series. Our simulations run by default to final time $T_f = 10$, however they can be prolonged as described in section III A. If the final time of the time series is larger than 10, then the cutoff time is 10, otherwise it is 1. Then, the input matrix (60) is built and separated into X and Y . After that, candidates for a possible rank of X are determined by the following procedure. We consider all singular values σ_k , $k = 1, \dots, K$ of X normalized by σ_1 with K being the smallest index corresponding to $\sigma_{K+1} < 10^{-10}$. Then if $\sigma_{k+1}/\sigma_k < 0.95$ for some k , then k is added to the list of possible ranks as there is a sufficient gap between σ_k and σ_{k+1} , which indicates that σ_{k+1} is a spurious singular value. For each rank from the list of all possible ranks we determine DMD decomposition and compute the fit and residual errors (59). Then we consider two smallest fit errors $e_{\text{DMD},1}$ and $e_{\text{DMD},2}$, and if $0.5 \leq e_{\text{DMD},1}/e_{\text{DMD},2} \leq 1$, then we also take into account corresponding residual errors, so that the DMD decomposition corresponding to the smallest residual error is considered the best. Otherwise, the best one corresponds to the decomposition with the fit error $e_{\text{DMD},1}$. Once the best-rank DMD is determined, its eigenvalues that have the real part larger than -1 and positive imaginary part are saved as an output of the postprocessing algorithm sorted by the frequency and real part, so that the enumeration of modes is the same as in the normal-mode analysis.

Example	$\hat{\alpha}_{\text{re}}$	$\hat{\alpha}_{\text{im}}$	e_{re}	e_{im}
1	3.00	2.00	1.91×10^{-14}	4.80×10^{-14}
	0.70	0.10	1.33×10^{-11}	3.51×10^{-12}
	0.80	1.57	4.19×10^{-13}	4.21×10^{-14}
2	0.60	2.76	1.42×10^{-12}	5.87×10^{-13}
	0.50	3.88	4.69×10^{-12}	1.04×10^{-12}
	0.01	15.62	1.08×10^{-07}	1.16×10^{-10}

Table I. Results of applying the postprocessing algorithm to synthetic data (61) (Example 1) and (62) (Example 2). Columns 2 and 3 show found growth rates and frequencies, respectively; columns 4 and 5 show the relative errors of growth rates and frequencies, respectively, computed using (64).

3. Testing the method with synthetic data

Now we apply the postprocessing algorithm to two synthetic time series chosen to represent typical unstable behavior of the solutions of system (44–45).

Example 1. Time series has a single exponentially growing and oscillating mode,

$$y_1(t) = A \exp(\alpha_{\text{re}} t) \sin(\alpha_{\text{im}} t), \quad (61)$$

where $\alpha = \alpha_{\text{re}} + i\alpha_{\text{im}} = 3 + 2i$, i being imaginary unit, $t \in [0; 51]$.

Example 2. Time series is a superposition of five exponentially growing and oscillating modes of different growth rates and frequencies,

$$y_2(t) = \sum_{i=0}^4 A \exp(\alpha_{\text{re},i} t) \sin(\alpha_{\text{im},i} t), \quad (62)$$

where $\alpha \in \{0.7 + 0.1i, 0.8 + 1.57i, 0.6 + 2.76i, 0.5 + 3.88i, 0.01 + 15.62i\}$, $t \in [0; 21]$. For both time series, the amplitude of each mode is taken as $A = 10^{-10}$, and the time step is $\Delta t = 0.01$. These time series are intentionally contaminated with a Gaussian noise of amplitude 10^{-13} , mean zero, and variance one such that the noise is proportional to the signal:

$$y = y_{\text{clean}}(1 + \text{noise}), \quad (63)$$

where y_{clean} is a noiseless time series (either (61) or (62)). The added noise is to mimic the noise due to numerical simulation errors.

To assess the performance of the postprocessing algorithm, we measure relative errors of extracted growth rates and frequencies. For example, if one particular mode in a time series has an exact eigenvalue α while the postprocessing algorithm finds a corresponding approximate eigenvalue $\hat{\alpha}$, then the errors are defined as

$$e_{\text{re}} = \frac{|\alpha_{\text{re}} - \hat{\alpha}_{\text{re}}|}{\alpha_{\text{re}}}, \quad e_{\text{im}} = \frac{|\alpha_{\text{im}} - \hat{\alpha}_{\text{im}}|}{\alpha_{\text{im}}}. \quad (64)$$

In Table I, we show the obtained modes along with the relative errors. As can be seen, the algorithm was able to recover all the modes present in the time series. We find that in general e_{re} is at least one order of magnitude larger than e_{im} . Nevertheless, the algorithm was able to recover in the Example 2 the slowest growing mode (with growth rate 0.01), albeit with a larger relative error than for the other modes, even though the growth rate of this mode is 80 times smaller than the growth rate of the dominant mode $\alpha = 0.8 + 1.57i$.

These examples demonstrate that the postprocessing algorithm we use is able to extract stability spectra from time series consisting of several modes of very different growth rates and frequencies. That said, it must be clear that there are also limitations to the procedure: the quality of the extracted spectrum in general depends on the quality of the time series at hand (its sampling rate, length, noise level, etc.).

As the Fourier transform and power spectra are frequently used in analysis of oscillatory dynamics, here we contrast this traditional method with the present approach. Applying the fast Fourier transform (FFT) to the time series, one can determine approximate values of frequencies of the modes via the power spectrum and then use nonlinear least-squares solver to find growth rates of the

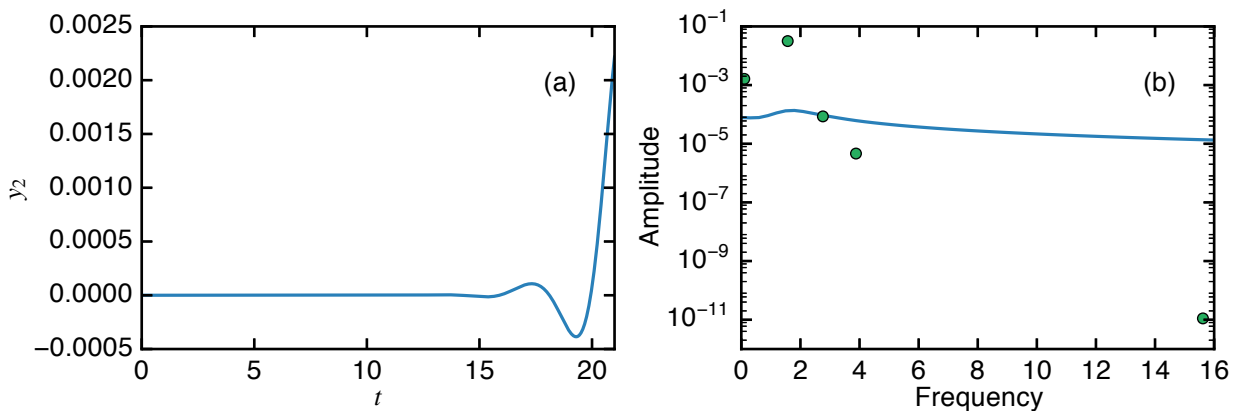


Figure 2. Comparison of FFT and DMD algorithms for analysis of time series (62): (a) the time series; (b) the power spectra by FFT (solid line; here the frequencies are multiplied by 2π) and DMD (markers).

modes. However note that for exponentially growing or decaying oscillations, FFT analysis may be too inaccurate. To illustrate, Figure 2 shows the time series (62) and its power spectra generated via FFT and DMD. While the DMD spectrum is sparse and is in excellent agreement with the time series, the FFT spectrum is seen to be essentially flat and dense in the sense that it is hard to find the particular modes present in the time series.

The algorithm for extracting growth rates and frequencies of unstable modes presented in this section requires multiple application of DMD to find the best low-rank approximation. However, the most expensive operation in the algorithm (SVD of X) is carried out only once. Our postprocessing code is based on the Intel Math Kernel Library, which contains optimized routines for numerical linear algebra. The time that it takes to postprocess our data varies as it is a function of the length of the time series and the number of possible ranks. The typical time on a workstation with a Xeon processor is on the order of a minute. Besides, as we process only one-dimensional time series (54), without having to save the full solution on the numerical grid for each time step, there is a substantial saving in terms of disk space and corresponding input-output operations.

IV. STABILITY RESULTS

We now apply the numerical algorithm developed above to the detonation problem with two different reaction-rate mechanisms. In Subsection IV A, we consider the conventional detonation model based on the Arrhenius heat-release rate. This model is widely used in detonation theory, in particular for stability analysis, since the pioneering works of Zel'dovich [69], von Neumann [66], Döring [13], and Erpenbeck [19, 42, 55, 58]. We use the results of normal-mode analysis from [42] and [55] for verification purposes. In Subsection IV B, we analyze the case of detonation with one exothermic and one endothermic reactions, and where possible compare our results with those obtained by normal-mode analysis [55].

A. One-step chemistry

The reaction rate is given by the Arrhenius form, $\omega = k(1 - \lambda) \exp(-E/RT)$. The stability of the steady-state self-sustained solutions for this model depends on the values of E , Q , and γ [19, 42]. Generally, increasing E has the effect of making the solution more unstable. The role of Q and γ is more complicated. For example, both very large and very small Q correspond to stable detonations while there is an instability at intermediate values of Q if E is large enough.

1. Steady-state solutions, eigenfunctions and eigenvalues

The steady-state traveling-wave solutions of (2-5) are found by setting the time derivatives in the system to zero. In figure 3, we show such ZND solution profiles computed with fixed parameters $\gamma = 1.2$ and $E = 30$, and for $Q = \{0.5, 1, 10, 50, 100\}$. For this particular value of E , the case $Q = 50$ corresponds to a strongly unstable solution, while all other values of Q correspond to stable

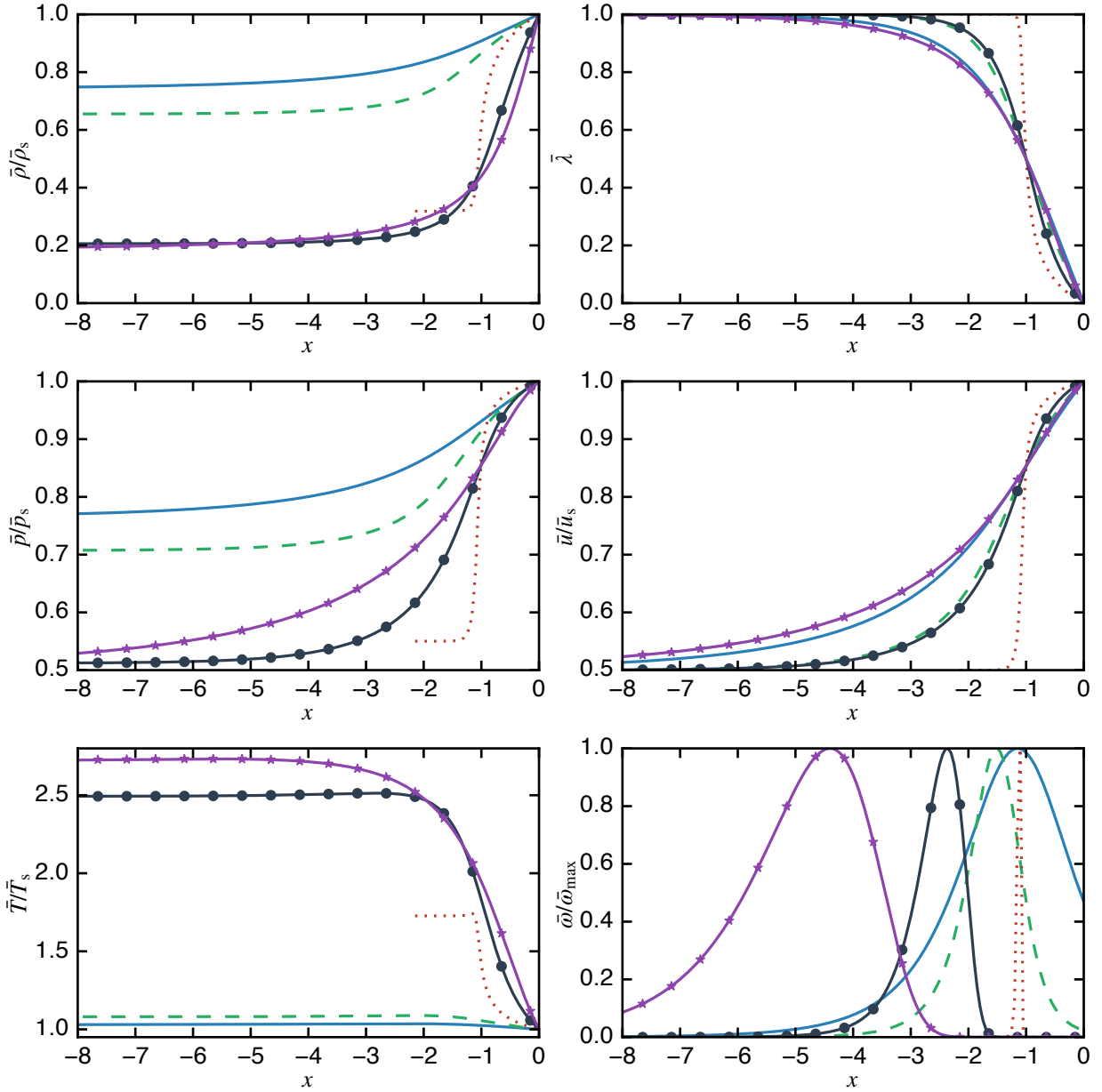


Figure 3. The steady solution with fixed $\gamma = 1.2$, $E = 30$, and various values of heat release: $Q = 0.5$ - solid, $Q = 1.0$ - dashed, $Q = 10$ - dotted, $Q = 50$ - solid with circles, $Q = 100$ - solid with stars. Density, pressure, velocity in the laboratory frame, and temperature are normalized by their respective values at the von Neumann (shock) state; the reaction rate is normalized by its maximum value.

or weakly unstable solutions. As can be seen from the steady-state profiles, the strongly unstable case occurs for the ZND solution approaching a square-wave shape with a spiky heat-release zone, while all the other cases correspond to relatively smooth profiles. This effect of the steady-state solutions on their stability is well known. The limiting case of a true square-wave detonation with instantaneous heat release is known to possess a pathological spectrum with infinite number of unstable eigenvalues with growth rates increasing unboundedly with the mode number (or its frequency). In other words, the square-wave stability problem is ill-posed. However, with a finite-rate chemistry, the problem remains well-posed even though the sharper the heat-release rate the larger the number of unstable modes and the larger their growth rates and frequencies. Computing the latter situations becomes a challenging problem.

Now we analyze the time series of the perturbation of detonation velocity, ψ' , for two cases that differ by the complexity of their unstable spectra. The parameters for these cases are $\gamma = 1.2$, $Q = 50$, and $E = 35$ or $E = 40$. Linear stability analysis [55] predicts that both of these cases have several unstable modes. In addition, the fundamental mode for the second case is purely exponential and has two branches.

E	i	α_{re}	e_{re}	α_{im}	e_{im}
35	0	0.42323	3×10^{-11}	0.17957	2×10^{-10}
	1	0.50528	1×10^{-11}	4.36602	1×10^{-13}
	0.0	0.18851	3×10^{-03}	0.00000	2×10^{-16}
40	0.1	1.00847	5×10^{-12}	0.00000	2×10^{-16}
	1	1.01845	2×10^{-12}	4.30457	3×10^{-13}
	2	0.67850	8×10^{-09}	7.90388	3×10^{-10}
	3	0.18504	4×10^{-03}	11.43653	6×10^{-05}

Table II. Unstable spectra for $\gamma = 1.2$, $Q = 50$, and $E = 35$ or $E = 40$ obtained from simulations with $N_{1/2} = 1280$. Here, i is the mode number; α_{re} and α_{im} are the growth rates and frequencies, respectively; e_{re} and e_{im} are the corresponding relative errors computed from the results with $N_{1/2} = 640$ and $N_{1/2} = 1280$.

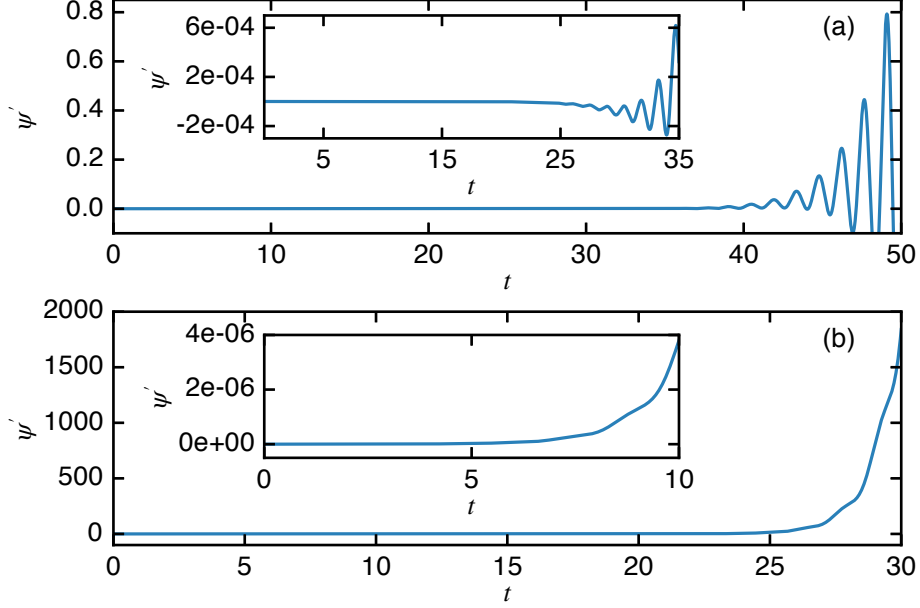


Figure 4. Computed time series of the perturbation of detonation velocity ψ' for $\gamma = 1.2$, $Q = 50$, and (a) $E = 35$ or (b) $E = 40$. Insets show the evolution of ψ' at early time of simulation.

Simulations are conducted with $T_f = 50$ for $E = 35$ and $T_f = 40$ for $E = 40$. Figure 4 displays the computed time series, with insets showing the solution at early times. The plots suggest that for $E = 35$ all modes are oscillatory, while for $E = 40$ an exponential nonoscillatory growth is present. Table II shows the unstable spectra for both of these cases obtained with $N_{1/2} = 1280$ as well as relative errors calculated by comparing the modes found with $N_{1/2} = 640$ and $N_{1/2} = 1280$. For the case $E = 40$, the number of modes found is the same as shown on figure 6 of [55]. The fundamental mode is purely exponential and is split in two branches in agreement with [55] where the author notes that the split occurs for $E \geq 35.86$. The growth rate of the upper branch of the fundamental mode is 1.008 in our calculations while it is 1.021 in [55] (extracted from figure 6 of [55] and rescaled to the Erpenbeck scales).

During the integration of the linearized system (12–15) we obtain the spatial profiles of the perturbations that are superpositions of the eigenfunctions of the problem. Such profiles are shown in Figure 5 at $E = 30$ and at three values of Q , two of which are near the neutral curve and one somewhere in the middle of the unstable domain. These are $Q = 1$ (stable), $Q = 10$ (strongly unstable), and $Q = 50$ (weakly unstable).

2. Comparison with normal-mode results

Here, we show a quantitative comparison with the normal-mode results found in the literature. As other researchers provide explicit values for unstable spectra for parameters $\gamma = 1.2$, $Q = 50$, we take these parameters as well and vary activation energy

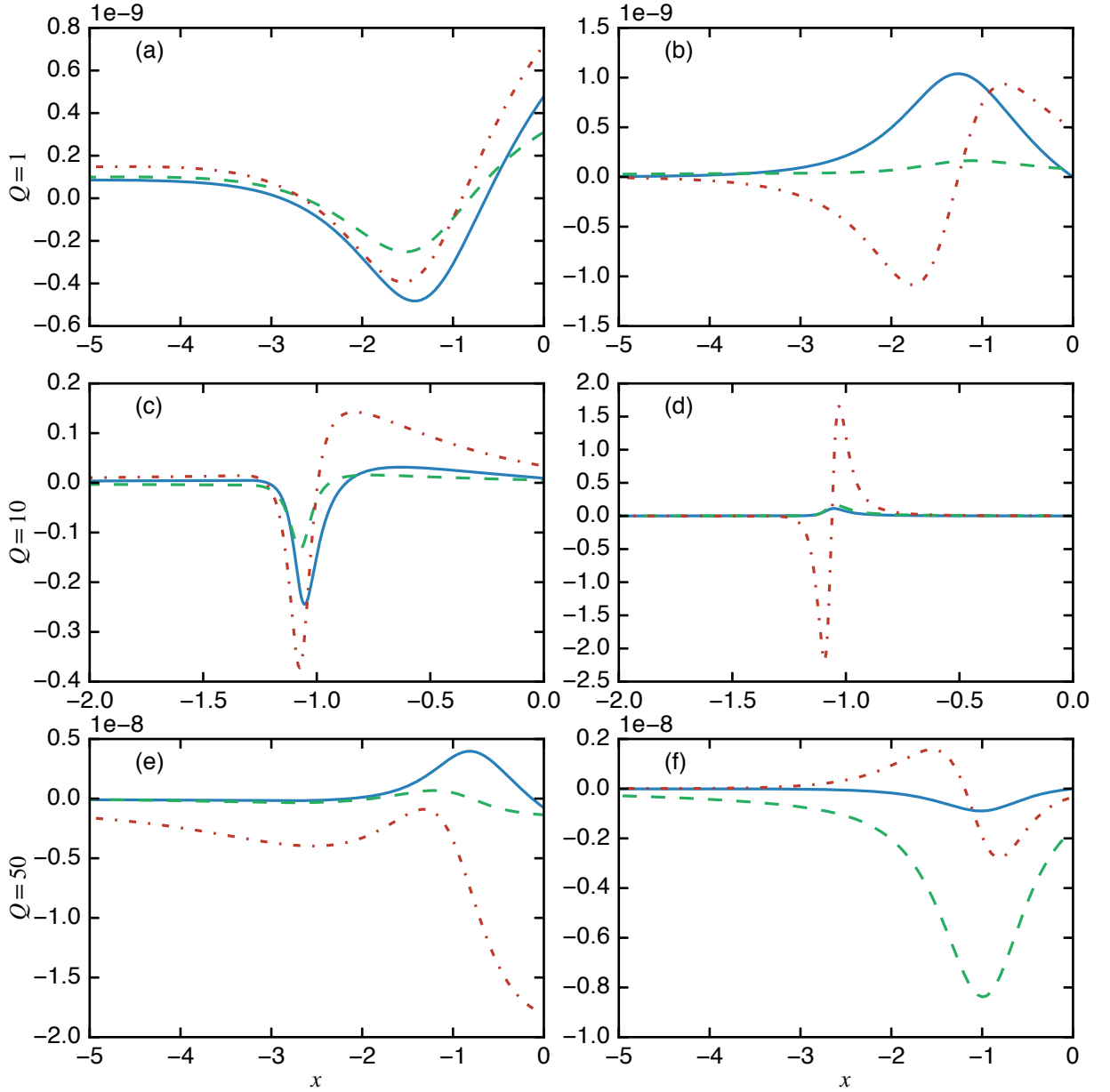


Figure 5. Perturbation profiles versus x for $E = 30$ and (a-b) $Q = 1$, (c-d) $Q = 10$, (e-f) $Q = 50$. Left column: ρ' (solid), u' (dashed), p' (dash-dotted); right column: λ' (solid), T' (dashed), ω' (dash-dotted). These solutions are plotted at a particular time, hence the scales are arbitrary.

E . Table III shows the results of the comparison. Our results are in agreement with the normal-mode results to at least two significant digits for all considered cases. The normal-mode results are borrowed from the work of different researchers: [55] for $E = 25.26$ and $E = 31.05$, from [26] for $E = 26$, and from [42] for $E = 50$. These researchers all used different scales, which are converted here to the same scales for comparison. We choose to convert to the Erpenbeck scales used in the present work. The conversion factors are as follows. Conversion factor from the scales of [55] to the Erpenbeck scales is nondimensional \bar{D} in the Erpenbeck scales, which is 6.809475 for $\gamma = 1.2$ and $Q = 50$. In [42], the stability spectrum for $E = 50$ is given in scales of [1], and the following conversion factor should be used:

$$\frac{k}{\int_0^{1/2} (1 - \bar{\lambda})^{-1} \exp(\bar{\rho}E/\bar{p}) d\bar{\lambda}},$$

where k is the nondimensional Arrhenius rate constant computed using (23), and the integral in the denominator is the nondimensional Arrhenius rate constant in the scales of [1]. For $\gamma = 1.2$, $Q = 50$, and $E = 50$, the numerical value of this factor is

E	i	Present work				Normal-mode analysis	
		α_{re}	e_{re}	α_{im}	e_{im}	α_{re}	α_{im}
25.26*	0	-0.00017	1×10^{-04}	0.53048	6×10^{-08}	0.000	0.530
26**	0	0.03709	5×10^{-09}	0.52215	5×10^{-11}	0.0371	0.52215
31.05*	0	0.26756	1×10^{-10}	0.40280	3×10^{-10}	N/A	N/A
	1	-0.00060	2×10^{-08}	4.37774	1×10^{-12}	0.00	4.38
50***	0.0	0.09365	3×10^{-07}	0.00000	2×10^{-16}	0.084	0.000
	0.1	1.74458	2×10^{-11}	0.00000	2×10^{-16}	1.743	0.000
	1	1.76536	6×10^{-11}	4.10817	1×10^{-12}	1.764	4.104
	2	1.77399	6×10^{-12}	7.83005	2×10^{-11}	1.772	7.823
	3	1.67745	1×10^{-09}	11.42106	1×10^{-10}	1.676	11.42
	4	1.53541	1×10^{-08}	14.99313	4×10^{-10}	1.534	14.98
	5	1.34788	4×10^{-08}	18.55077	6×10^{-10}	1.346	18.53
	6	1.14096	1×10^{-07}	22.10524	7×10^{-10}	1.140	22.09
	7	0.91468	5×10^{-07}	25.65854	2×10^{-10}	0.913	25.64
	8	0.67788	1×10^{-06}	29.21139	2×10^{-09}	0.677	29.19
9	0.43092	4×10^{-06}	32.76403	5×10^{-09}	0.431	32.73	
10	0.17764	2×10^{-05}	36.31692	1×10^{-08}	0.177	36.28	

Table III. Comparison of the unstable spectra between the present work and the normal-mode results for $\gamma = 1.2$ and $Q = 50$. Sources for the normal-mode results: *[55, p. 2617]; **[26, p. 321]; ***[42, p. 127] except mode 0.0 which is extracted from [58, figure 6]. Here, i is the mode number. For $E = 50$ the fundamental mode has two branches, which we denote with 0.0 and 0.1. Eigenvalues α are in the scales used in the present work. Notice that the errors are computed using grid refinement.

0.938749. Conversion of results of [26] is not needed because they provide the stability spectrum in the same scales as ours.

To obtain the results shown in Table III, we run the simulations to final time $T_f = 30$ for $E = 25.26$ and $E = 26$ and to $T_f = 10$ for $E = 31.05$ and $E = 50$. The simulations are conducted with resolutions $N_{1/2} = 20, \dots, 1280$ with refinement factor 2 to verify the convergence of the obtained stability spectra, which is observed as expected. Table III shows the spectra obtained with $N_{1/2} = 1280$. The errors on growth rates and frequencies are also shown in Table III. They are computed using:

$$e_{re} = \left| \frac{\alpha_{re,1} - \alpha_{re,2}}{\alpha_{re,2}} \right|, \quad e_{im} = \left| \frac{\alpha_{im,1} - \alpha_{im,2}}{\alpha_{im,2}} \right|,$$

where subscripts 1 and 2 denote quantities obtained with $N_{1/2} = 640$ and $N_{1/2} = 1280$, respectively.

3. Neutral stability curves

Next, we use the present method to generate neutral stability curves in E - Q plane for various γ . The corresponding algorithm is as follows. Assuming that instability monotonically increases as E increases, the idea of bisection is used to find a critical value of E for each given Q such that the growth rate of a given mode is close to zero with tolerance 10^{-4} . Initial interval of search for E is taken [10; 140] for all results shown in this section. Grid resolution used here is $N_{1/2} = 40$.

Figure 6 displays the comparison between our results and those of [42] for the fundamental mode and $\gamma = 1.2$. It can be seen that there is a good agreement between the results. In Figure 7(a), the neutral stability curves of mode 0 in E - Q plane are shown for various γ , while in Figure 7(b), the frequency of neutral oscillation is shown. The smaller values of γ are seen to extend the range of unstable E to smaller E when Q is larger than about 4, and to reduce the unstable range towards larger values of E at $Q \lesssim 4$. At the same time, the frequency of neutral oscillation is seen to decrease substantially with decreasing γ at large Q , while it is essentially independent of γ at small values of Q . However, for small Q frequency exhibits nonmonotonic behavior for all γ except $\gamma = 1.4$.

For $\gamma = 1.2, 1.3$, and 1.4 neutral stability curves shown in Figure 7(a) represent stability boundaries for corresponding γ , which separate stable ZND solutions from unstable ones. However, the case $\gamma = 1.1$ is more complicated as for $3.7 \lesssim Q \lesssim 36$ mode 1 is more unstable than the fundamental mode. A typical time series of the perturbation of detonation velocity ψ' for such situation is shown in Figure 8 for $Q = 30.473$ and $E = 12.503$, which corresponds to the mode 0 being neutrally stable (its growth rate is about -10^{-6}) while mode 1 grows with a rate about 0.03. Figure 9 shows neutral stability curves for both mode 0 and 1 for $\gamma = 1.1$ on the same plot, where it can be clearly seen that the neutral stability boundary is determined by a composition of

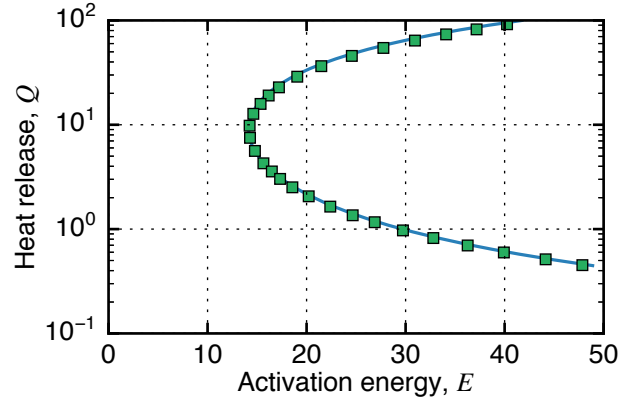


Figure 6. The neutral stability boundary computed with the present method (solid line) and its comparison with the normal-mode result of Lee and Stewart [42, figure 7] (square markers).

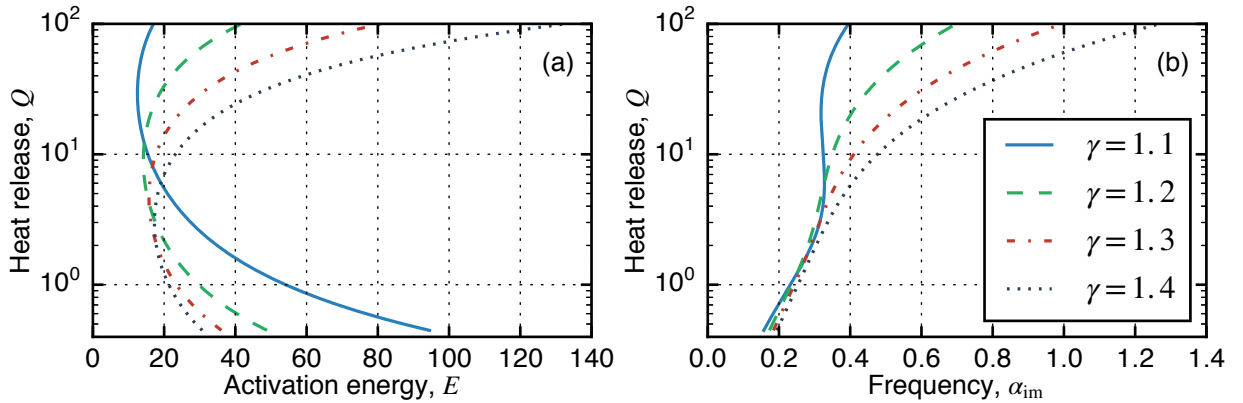


Figure 7. Neutral stability at various γ : (a) neutral stability boundary in E - Q plane, (b) frequency of oscillation along the neutral stability boundary.

the neutral stability curves of these two modes. This intersection of neutral curves at $\gamma = 1.1$ was not mentioned before in the literature, to the best of our knowledge.

B. Two-reaction model

The model with two reactions represents an example of complex chemistry that brings in the following additional complications that are absent in the one-step model. First, we now have two traveling-wave solutions for the same set of parameters of the problem, and therefore we must investigate the stability of both. Second, the solution has an embedded sonic point, that is the sonic condition is reached at a finite distance from the lead shock. This divides the post-shock flow into two regions that play distinct roles in the detonation dynamics. Following prior research on the role of sonic points in unsteady detonation dynamics [32, 59], we expect that the dynamics is affected only by the solution between the shock and the sonic point. How exactly this idea plays out in the linear stability calculations is not obvious, and this will be explored in this section.

1. Steady-state solutions and perturbations

Now the model has several additional parameters coming from the more complex chemistry. Comprehensive investigation of the entire parameter space would be a difficult task. Instead, we focus here on particular questions that have certain physical interest. Namely, we investigate how the level of endothermicity affects stability, and in addition, we compare stability behavior of the two steady-state solutions that co-exist at the same parameter set.

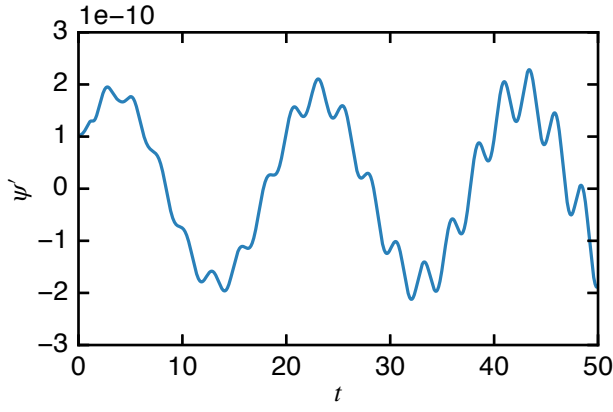


Figure 8. Example time series of ψ' for $\gamma = 1.1$, in which mode 0 is neutrally stable while mode 1 is unstable.

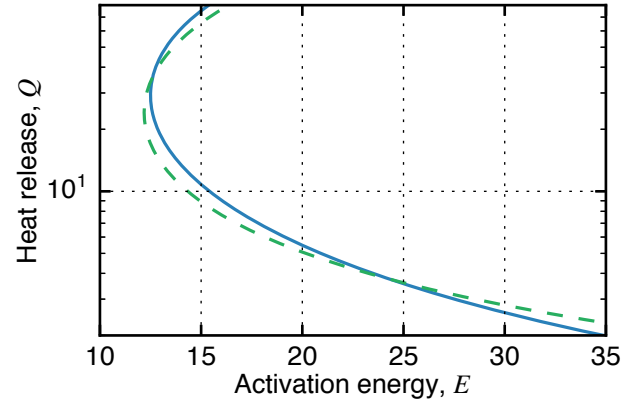


Figure 9. Neutral stability curves for $\gamma = 1.1$ for modes 0 (solid line) and 1 (dashed line).

First, we study the behavior of ZND solutions when Q_2 is varied while all other parameters are kept fixed. Figure 10 shows profiles of ZND variables $\bar{\rho}$, \bar{u} , \bar{p} , \bar{T} , $\bar{\lambda}_1$, and $\bar{\lambda}_2$ for subsonic-supersonic case with $\gamma = 1.2$, $Q_1 = 50$ and $E = 25$ for several values of Q_2 , obtained with $N_{1/2} = 40$. As can be seen from the figure, the lower the values of Q_2 , the larger the gradients of the profiles become. The maximum temperature decreases with increasing magnitude of Q_2 , as expected.

Figure 11 displays the same results as in Figure 10, but for subsonic-subsonic solution, which is obtained now with $N_{1/2} = 640$ to accurately resolve the weak discontinuity in the solution. It can be seen that as the magnitude of Q_2 increases, and the sonic point moves toward the shock, the kink in the profiles of $\bar{\rho}$, \bar{u} and \bar{p} becomes more pronounced.

Now we consider the behavior of the perturbation profiles $z'(x, t) = \{\rho', u', p', \lambda'_1, \lambda'_2\}$ taken at a particular time with $T_f = 4$. We take $\gamma = 1.2$, $E = 15$ and $Q_1 = \{10, 20, 50\}$ with $Q_2 = -0.75Q_1$. Figure 12 shows the perturbations for the subsonic-supersonic case, while Figure 13 for the subsonic-subsonic case. The most prominent distinction between the two figures is that, while profiles for the subsonic-supersonic case are smooth, profiles for the subsonic-subsonic case develop discontinuities at the sonic point caused by discontinuous coefficient matrices A and B in (44): ZND profiles themselves are continuous, their derivatives with respect to x have jump discontinuities at the sonic point, hence, discontinuous perturbations. In addition, we noticed that the upwind method (46–47) with Lax–Friedrichs flux led to severe Gibbs oscillations on both sides of the jump in the profiles of the subsonic-subsonic case. For this reason, we replaced the upwind method with the WENO method [28] for all simulations based on subsonic-subsonic case. Another important observation from comparing figures 12 and 13 is that perturbations are nearly the same in the region between the sonic point and the leading detonation shock: for example, the relative difference between density perturbations is only 1% in this region, and it is likely caused by the smearing of the discontinuities in the neighborhood of the sonic point.

2. Migration of spectra with increasing endothermicity

Here we investigate how the stability behavior changes as the endothermicity increases, that is as Q_2 increases in magnitude while all the other parameters are kept fixed.

First, consider the subsonic-supersonic case. We choose $N_{1/2} = 40$, $\gamma = 1.2$, $E = 25$, $Q_1 = 50$ and let Q_2 vary in the range $-45 \leq Q_2 \leq 0$ with step $\Delta Q_2 = 0.0025$ for $Q_2 \in [-0.7; -0.8] \cup [-13.9; -14] \cup [-19.9; -20] \cup [-25.2; -25.3]$ and step $\Delta Q_2 = 0.1$ otherwise. Figure 14 shows how growth rates change as Q_2 decreases. Initially, at $Q_2 = 0$ detonation corresponds to the equilibrium CJ case and is stable for γ , E and Q_1 that we use (critical value of activation energy is 25.26). As Q_2 decreases, the growth rate of the fundamental mode (mode 0) increases almost linearly such that at $Q_2 \approx -0.79$ detonation becomes unstable, and at $Q_2 \approx -25.2225$ mode 0 splits into two purely exponential branches, with growth rates increasing and decreasing for the top and bottom branches, respectively. At the same time at $Q_2 \approx -13.1$ the stable mode 1 appears in the spectrum, which becomes unstable at $Q_2 \approx -13.9425$. As the growth rate of this mode increases faster than that of mode 0, at $Q_2 \approx -19.92$ it becomes the dominant mode and remains so all the way down to $Q_2 = -45$. In total, up to six modes appear in the spectrum as $Q_2 \rightarrow -45$. Here we point out that taking $|Q_2|$ larger than 45 makes computations prohibitively expensive as the effective reaction lengths become hundreds of thousands of nondimensional units, because as $|Q_2| \rightarrow |Q_1|$ the overall heat release becomes effectively zero and detonation degenerates to an inert weak shock.

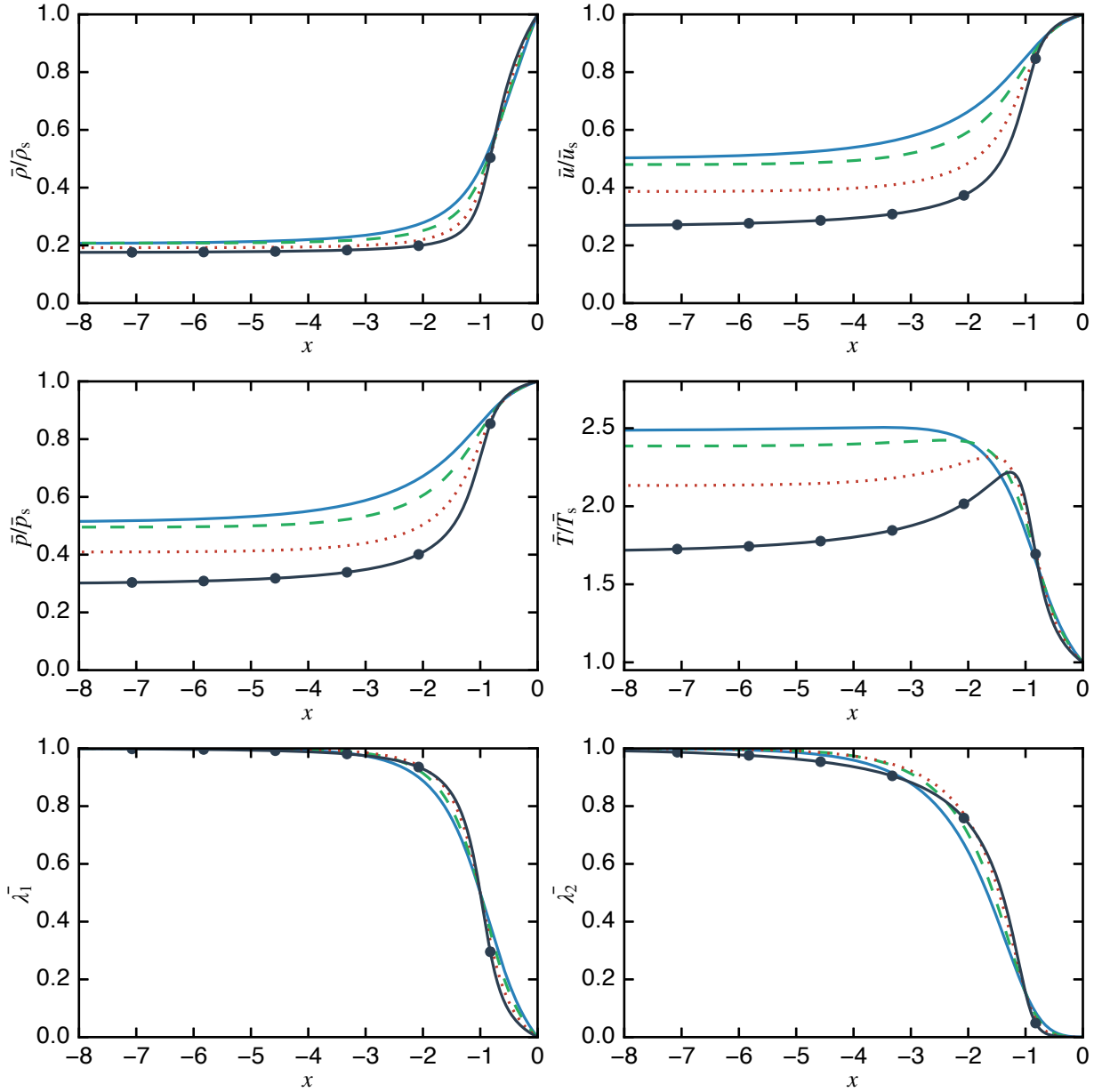


Figure 10. ZND subsonic-supersonic profiles of density $\bar{\rho}$, flow velocity \bar{u} , pressure \bar{p} , temperature \bar{T} , and progress variables $\bar{\lambda}_1$ and $\bar{\lambda}_2$ for $\gamma = 1.2$, $Q_1 = 50$, $E = 25$, and different values of Q_2 . Solid line corresponds to $Q_2 = -1$; dashed line to $Q_2 = -10$; dotted line to $Q_2 = -20$; solid line with circle markers to $Q_2 = -30$. Density, flow velocity, pressure, and temperature are normalized by their values on the shock.

Next, consider the subsonic-subsonic case. The physical parameters are taken the same as in the previous case. However, due to the discontinuous coefficients in the linearized system (44), now we must use drastically higher resolutions (here $N_{1/2} = 1280$) than for the subsonic-supersonic case. Otherwise, we are unable to extract low-energy modes. We also emphasize that it is significantly more difficult to postprocess the time series of perturbation of detonation velocity for the subsonic-subsonic case. The reason is that the time series contains substantial amount of numerical noise caused by the numerical smearing of the jump in the solution in the neighborhood of the sonic locus.

Figure 15 shows the spectra for subsonic-supersonic and subsonic-subsonic cases together. It can be seen that the spectra are close to each other. In fact, they are essentially indistinguishable for oscillatory part of mode 0, upper branch of exponential part of mode 0, and for modes 1, 2, and 3. However, for subsonic-subsonic case, the lower branch of exponential part of mode 0 shows significant numerical noise as Q_2 decreases. The same behavior is seen with mode 4 as well. The reason for this is that the discontinuity in the solutions for subsonic-subsonic case generates noise that contaminates time series of ψ' . As the lower branches of modes 0 and 4 contribute to the time series much less energy than other modes, they are more difficult to distinguish

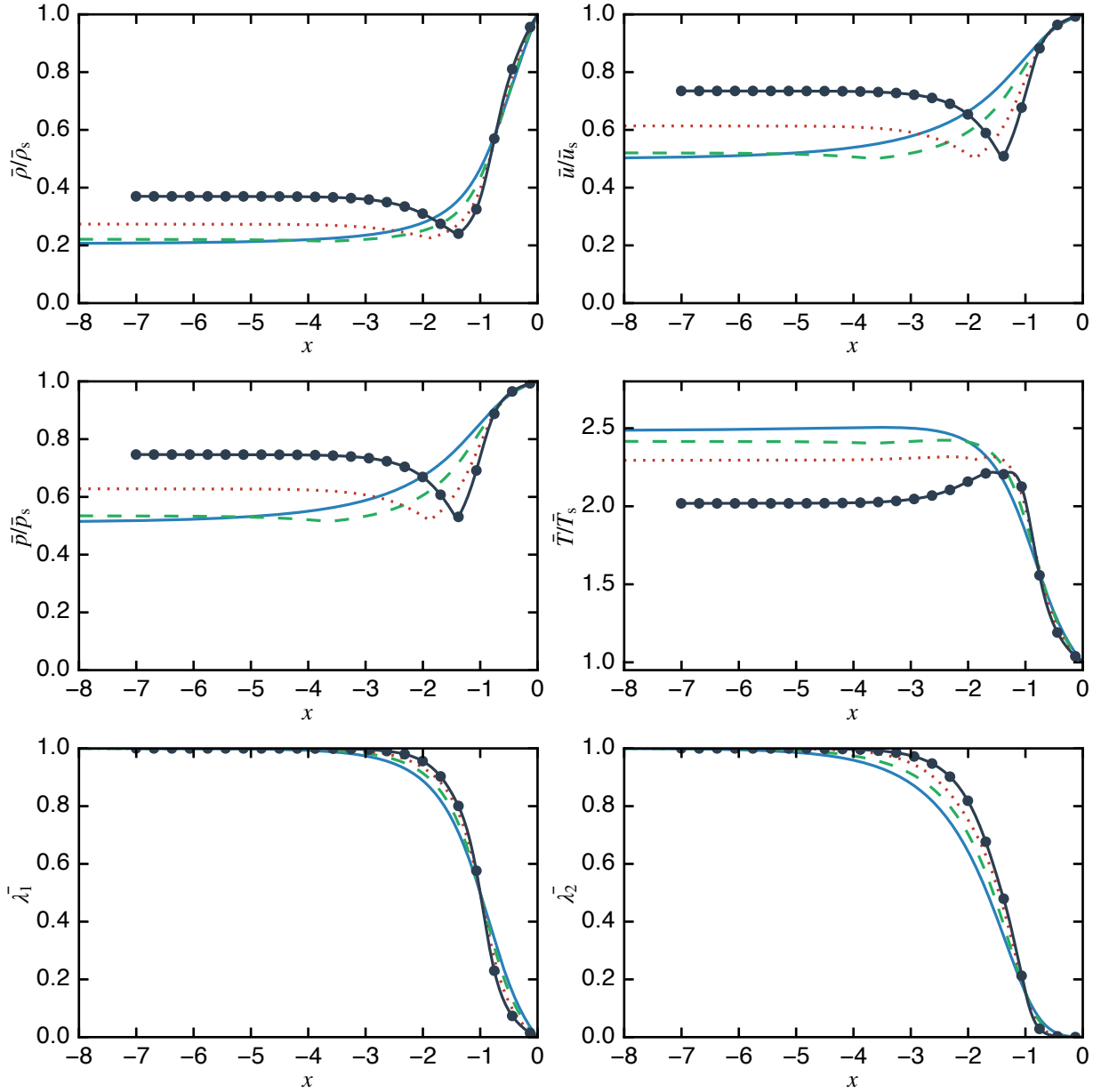


Figure 11. ZND subsonic-subsonic profiles of density $\bar{\rho}$, flow velocity \bar{u} , pressure \bar{p} , temperature \bar{T} , and progress variables $\bar{\lambda}_1$ and $\bar{\lambda}_2$ for different values of Q_2 . Solid line corresponds to $Q_2 = -1$; dashed line to $Q_2 = -10$; dotted line to $Q_2 = -20$; solid line with circle markers to $Q_2 = -30$. Density, flow velocity, pressure, and temperature are normalized by their values on the shock.

from the noise, which is an issue that can probably be fixed by using an improved algorithm for solving hyperbolic problems with discontinuous coefficients. Nevertheless, the computed values are near their counterparts for the subsonic-supersonic case. Despite some differences in the spectra, Figure 15 serves as a demonstration that stability of ZND solutions of the two-step model with endothermicity does not depend on whether the underlying ZND solution is of subsonic-supersonic or subsonic-subsonic case. That is, the detonation stability is apparently determined solely by the dynamics of the reaction zone between the sonic point and the leading detonation shock.

As a final note on this section, we give the reader an idea of the computational requirements for these calculations. For both subsonic-supersonic and subsonic-subsonic cases, the number of values of Q_2 we took is approximately 500. Then, as the resolution necessary for the subsonic-supersonic case is only $N_{1/2} = 40$, we were able to compute Figure 14 overnight on a workstation with 16 cores. In contrast, the subsonic-subsonic case requires much higher resolution of $N_{1/2} = 1280$, so these computations required a day with 512 parallel workers on a parallel computer, where a worker simulates and postprocesses results for a given Q_2 independently of other workers.

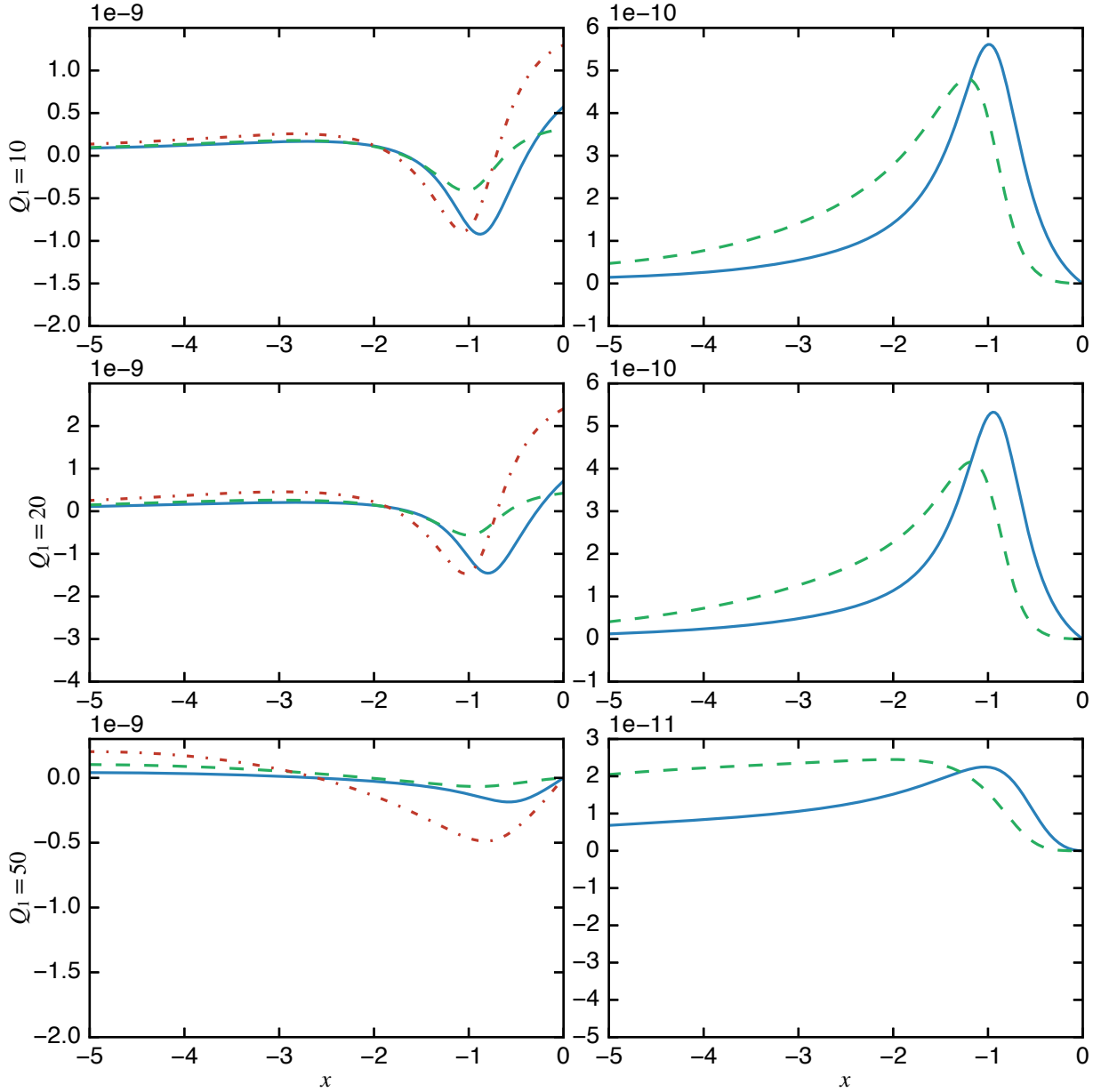


Figure 12. Perturbation profiles for the subsonic-supersonic case for $\gamma = 1.2$, $E = 15$, $Q_1 \in \{10, 20, 50\}$ with $Q_2 = -0.75Q_1$. On the left: solid line ρ' , dashed line u' , dash-dotted line p' . On the right: solid line λ_1' , dashed line λ_2' . Perturbations are not scaled and shown as they are at the simulation time $T_f = 4$. Notice, that the left limits of x -axes are taken to be 5 for clarity and are much smaller than the reaction lengths.

3. Neutral curves

In this section, we study how endothermicity affects the neutral stability boundary in comparison with the one-step model. The comparison is based on the idea that the detonation dynamics in both cases is determined by the energy released between the shock and sonic point. Therefore, the one-step model with heat release Q is compared with the two-step model with the maximum heat release Q^* equal to Q .

In Figure 16, we show the neutral stability curves in the parametric plane $E-Q$. We use $\gamma = 1.2$ and therefore the neutral stability curve for the one-step model is the same as in Figure 6. The neutral curve for the two-step model is obtained for the ZND solution corresponding to the subsonic-supersonic case. The range of Q_1 is $10^{-0.35}$ – $10^{2.35}$ with 256 logspaced points while Q_2 is varied in proportion to Q_1 : $Q_2 = -0.75Q_1$. For each Q_1 we find the critical value of E by the algorithm described earlier. For values of $10^{-0.35} \leq Q_1 \lesssim 0.8$ (approximately 20 points) the algorithm did not converge and we omit these values from the figure. The

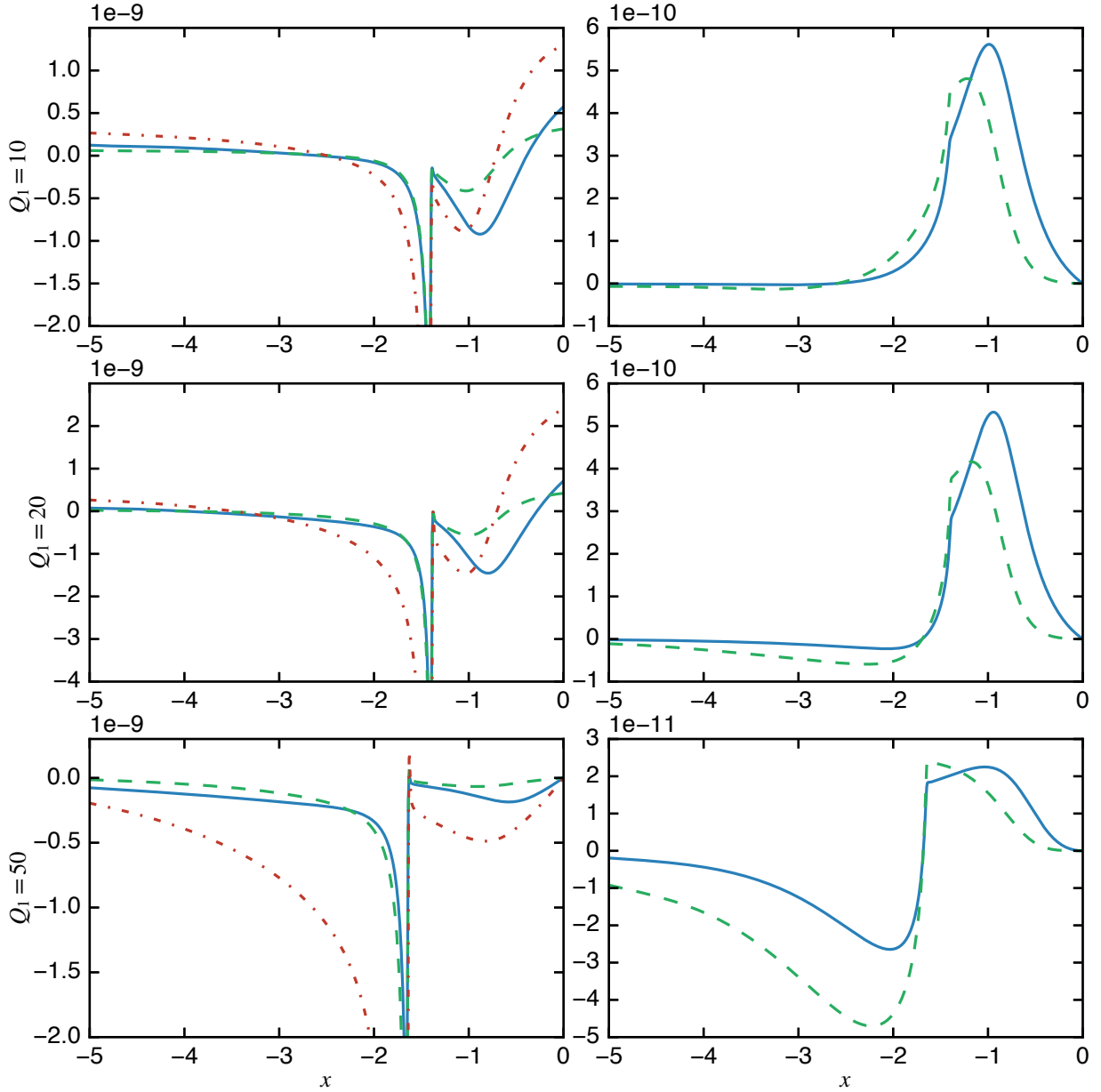


Figure 13. Perturbation profiles for the subsonic-subsonic case for $\gamma = 1.2$, $E = 15$, $Q_1 \in \{10, 20, 50\}$ with $Q_2 = -0.75Q_1$. On the left: solid line ρ' , dashed line u' , dash-dotted line p' . On the right: solid line λ_1' , dashed line λ_2' . Perturbations are not scaled and shown as they are at the simulation time $T_f = 4$. Notice, that the left limits of x -axes are taken to be 5 for clarity and are much smaller than the reaction lengths.

curves shown demonstrate that endothermicity consistently shifts the neutral stability boundary toward smaller values of E over the whole range of Q that we investigated. The difference ΔE between critical activation energies for two models behaves with varying Q as follows. The minimum value $\Delta E \approx 1.5$ is attained for $5 \lesssim Q \lesssim 15$. As Q increases, ΔE increases monotonically and reaches $\Delta E \approx 4.5$ as $Q \rightarrow 100$. For low values of Q , ΔE increases quickly and in the limit $Q \rightarrow 0$, $\Delta E \rightarrow \infty$ as the detonation wave becomes an inert shock. Additionally, while for the one-step model, all ZND solutions are stable at $E \leq 14.2$ for the full considered range of Q , for the two-reaction model all ZND solutions are stable for $E \leq 12.6$.

Thus, the two-step exothermic-endothermic heat release leads to an increased instability compared to the equivalent one-step heat release. In order to provide some qualitative explanation for this observation, we look at how the steady-state thermicity behaves for the same values of E and Q^* for the two models. The thermicity for the two-step model is given by $\bar{\sigma}_1 \bar{\omega}_1 + \bar{\sigma}_2 \bar{\omega}_2$, where $\bar{\sigma}_i = (\gamma - 1)Q_i / \bar{c}^2$, $i = 1, 2$. Figure 17 shows the thermicity profiles for $\gamma = 1.2$, $Q^* = 10$, and $E = 15$ which correspond to the unstable steady-state solutions from Figure 16. It is clear that for the two-step model the thermicity has significantly larger peak value which is in addition located closer to the lead shock than the value for the one-step model. Thus, a possible reason

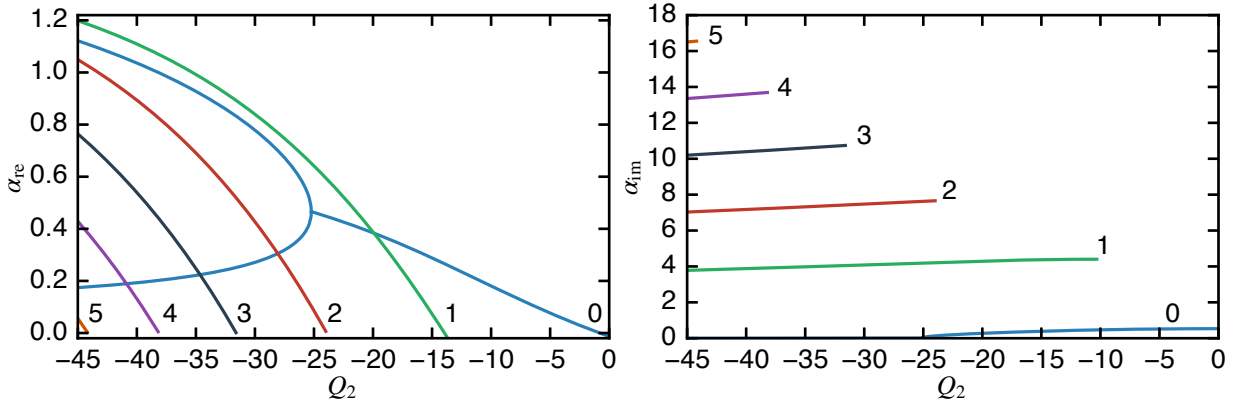


Figure 14. Growth rate versus Q_2 for $-45 \leq Q_2 \leq 0$ with other parameters $\gamma = 1.2$, $E = 25$, $Q_1 = 50$ for subsonic-supersonic case.

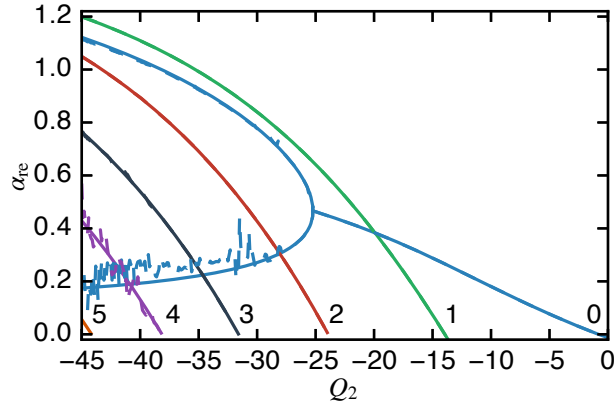


Figure 15. Growth rate versus Q_2 for $-45 \leq Q_2 \leq 0$ with $\gamma = 1.2$, $E = 25$, $Q_1 = 50$. Solid lines: subsonic-supersonic case, dashed lines: subsonic-subsonic case. Note that in most cases the solid and dashed curves overlap and are thus indistinguishable.

for the increased instability is this sharper profile of the thermicity function that makes for a more effective resonant cavity for the perturbations between the shock and the sonic point. Recall that the thermicity is a source term in the equation for the forward characteristics, $\dot{p} + \rho c \dot{u} = \rho c^2 (\sigma_1 \omega_1 + \sigma_2 \omega_2)$. As such it could be looked at as a measure of how the chemical reactions amplify the forward compression waves that influence the lead shock. The larger the magnitude of thermicity, the stronger the effect. The sharpness of the thermicity function reflects in the sensitivity of this influence on the changes in the local state in the reaction zone, the stronger sensitivity implying more instability. Obviously, these are qualitative arguments that require a rational analytical justification to be seen as a valid explanation, something that is outside the scope of this work.

V. CONCLUSIONS

In this work, we introduced a new approach to the problem of computing linear stability properties of detonation waves. The method consists of two parts. First is a numerical solution of the time-dependent linearized system of reactive Euler equations by a shock-fitting numerical algorithm. The result of such numerical calculation is an accurate time series of the detonation velocity for the linear problem. This solution is obtained only over relatively short time intervals which is computationally inexpensive. The second part of the method is an analysis of the obtained time series through the application of the method of Dynamic Mode Decomposition. As a result, we are able to calculate detailed stability properties of gaseous detonations with either one-step Arrhenius kinetics or two-step kinetics. Adding more chemical reactions requires essentially the same level of numerical and analytical effort for the computations. What distinguishes the proposed method from traditional normal-mode methods for detonations is that it does not require any special treatment of sonic points (which requires quite intricate analyses in the normal-mode methods). The numerical implementation of the method is relatively easy to generalize to more complex chemistry and equations of state.

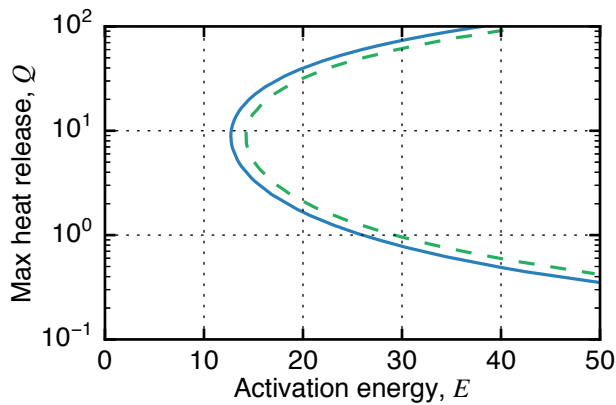


Figure 16. Neutral stability curves for two-step model with subsonic-supersonic steady-state solution (solid line) and one-step model (dashed line).

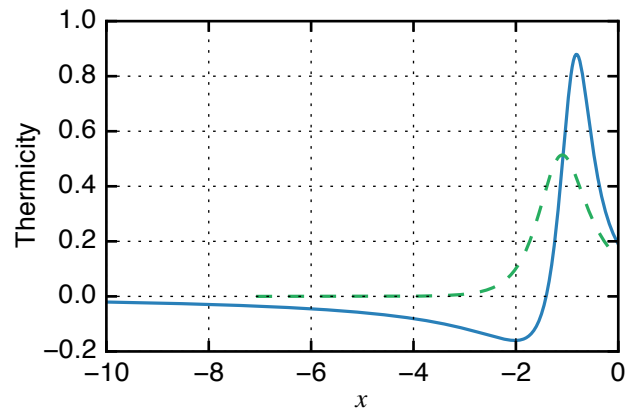


Figure 17. Thermicity profiles for $Q^* = 10$, $E = 15$ for two-step model with subsonic-supersonic steady-state solution (solid line) and one-step model (dashed line).

It is worth emphasizing that the methodology we presented in this work can be applied to any problem of shock wave stability. The key elements of the analysis (numerical solution of linearized equations and DMD processing of the computed shock velocity) are clearly independent of the specific details of the detonation problems that we investigated in this paper. What is important concerning detonation is that it possesses strong instabilities and is sensitive to details of numerical algorithms. As such, detonation represents a very stringent test problem that is rather demanding of any numerical methods used to compute its properties. We hope that the present method of stability analysis can be applied to a wide range of problems where shock wave dynamics is of importance.

ACKNOWLEDGEMENTS

This work was partially supported by the King Abdullah University of Science and Technology (KAUST) in Thuwal, Saudi Arabia. For computer time, this work used the resources of the Supercomputing Laboratory at KAUST. A. K. was also partially supported by the Russian Foundation for Basic Research (grant #17-53-12018).

-
- [1] G. Abouseif and T. Y. Toong. Theory of unstable one-dimensional detonations. *Combust. Flame*, 45:64–94, 1982.
 - [2] A. Alekseev, D. Bistrián, A. Bondarev, and I. Navon. On linear and nonlinear aspects of dynamic mode decomposition. *International Journal for Numerical Methods in Fluids*, 82(6):348–371, 2016.
 - [3] A. Alla and J. N. Kutz. Nonlinear model order reduction via dynamic mode decomposition. *SIAM Journal on Scientific Computing*, 39(5):B778–B796, 2017.
 - [4] H. Arbabi and I. Mezić. Study of dynamics in unsteady flows using Koopman mode decomposition. *arXiv preprint arXiv:1704.00813*, 2017.
 - [5] S. Bagheri. Effects of weak noise on oscillating flows: linking quality factor, floquet modes, and koopman spectrum. *Physics of Fluids*, 26(9):094104, 2014.
 - [6] B. Barker, R. Nguyen, N. Ventura, and C. Wahl. Computing Evans functions numerically via boundary-value problems. *arXiv preprint arXiv:1710.02500*, 2017.
 - [7] J. W. Bates and D. C. Montgomery. The D’yakov-Kontorovich instability of shock waves in real gases. *Physical Review Letters*, 84(6):1180, 2000.
 - [8] P. N. Brown, G. D. Byrne, and A. C. Hindmarsh. VODE: A variable-coefficient ODE solver. *SIAM journal on scientific and statistical computing*, 10(5):1038–1051, 1989.
 - [9] B. W. Brunton, L. A. Johnson, J. G. Ojemann, and J. N. Kutz. Extracting spatial–temporal coherent patterns in large-scale neural recordings using dynamic mode decomposition. *Journal of neuroscience methods*, 258:1–15, 2016.
 - [10] S. L. Brunton, B. W. Brunton, J. L. Proctor, E. Kaiser, and J. N. Kutz. Chaos as an intermittently forced linear system. *Nature Communications*, 8, 2017.

- [11] K. K. Chen, J. H. Tu, and C. W. Rowley. Variants of dynamic mode decomposition: boundary condition, Koopman, and Fourier analyses. *Journal of Nonlinear Science*, 22(6):887–915, 2012.
- [12] S. T. M. Dawson, M. S. Hemati, M. O. Williams, and C. W. Rowley. Characterizing and correcting for the effect of sensor noise in the dynamic mode decomposition. *Experiments in Fluids*, 57(3):1–19, 2016.
- [13] W. Döring. Über den detonationvorgang in gasen. *Annalen der Physik*, 43(6/7):421–428, 1943.
- [14] P. G. Drazin and W. H. Reid. *Hydrodynamic stability*. Cambridge university press, 2004.
- [15] D. Duke, J. Soria, and D. Honnery. An error analysis of the dynamic mode decomposition. *Experiments in Fluids*, 52(2):529–542, 2012.
- [16] S. P. D’yakov. The stability of shock waves. *Journal of Experimental and Theoretical Physics*, 27(3):288–296, 1954.
- [17] G. A. El and M. A. Hoefer. Dispersive shock waves and modulation theory. *Physica D: Nonlinear Phenomena*, 333:11–65, 2016.
- [18] J. J. Erpenbeck. Stability of step shocks. *The Physics of Fluids*, 5(10):1181–1187, 1962.
- [19] J. J. Erpenbeck. Stability of idealized one-reaction detonations. *Phys. Fluids*, 7:684–696, 1964.
- [20] R. Fernández and C. Thompson. Stability of a spherical accretion shock with nuclear dissociation. *The Astrophysical Journal*, 697(2):1827, 2009.
- [21] W. Fickett and W. C. Davis. *Detonation: theory and experiment*. Dover Publications, 2011.
- [22] T. Foglizzo, P. Galletti, L. Scheck, and H.-T. Janka. Instability of a stalled accretion shock: evidence for the advective-acoustic cycle. *The Astrophysical Journal*, 654(2):1006, 2007.
- [23] G. R. Fowles and G. W. Swan. Stability of plane shock waves. *Physical Review Letters*, 30(21):1023, 1973.
- [24] N. Golyandina and A. Zhigljavsky. *Singular Spectrum Analysis for time series*. Springer Science & Business Media, 2013.
- [25] E. Hairer, S. P. Nørsett, and G. Wanner. *Solving Ordinary Differential Equations I: Nonstiff problems*. Springer, 1993.
- [26] A. K. Henrick, T. D. Aslam, and J. M. Powers. Simulations of pulsating one-dimensional detonations with true fifth order accuracy. *J. Comput. Phys.*, 213(1):311–329, 2006.
- [27] J. Humpherys and K. Zumbrun. Efficient numerical stability analysis of detonation waves in ZND. *arXiv preprint arXiv:1011.0897*, 2010.
- [28] G. Jiang and D. Peng. Weighted ENO Schemes for Hamilton-Jacobi Equations. *SIAM J. Sci. Comput.*, 21(6):2126–2143, 2000.
- [29] M. R. Jovanović, P. J. Schmid, and J. W. Nichols. Sparsity-promoting dynamic mode decomposition. *Physics of Fluids*, 26(2):024103, 2014.
- [30] A. R. Kasimov. *Theory of instability and nonlinear evolution of self-sustained detonation waves*. PhD thesis, University of Illinois at Urbana-Champaign, Urbana, IL, USA, 2004.
- [31] A. R. Kasimov and D. S. Stewart. Spinning instability of gaseous detonations. *J. Fluid Mech.*, 466:179–203, 2002.
- [32] A. R. Kasimov and D. S. Stewart. On the dynamics of self-sustained one-dimensional detonations: A numerical study in the shock-attached frame. *Physics of Fluids*, 16:3566, 2004.
- [33] A. R. Kasimov and D. S. Stewart. Asymptotic theory of evolution and failure of self-sustained detonations. *J. Fluid Mech.*, 525:161–192, 2005.
- [34] W.-T. Kim, Y. Kim, and J.-G. Kim. Nature of the wiggle instability of galactic spiral shocks. *The Astrophysical Journal*, 789(1):68, 2014.
- [35] V. M. Kontorovich. Concerning the stability of shock waves. *Soviet Phys. JETP*, 6, 1958.
- [36] B. O. Koopman. Hamiltonian systems and transformation in hilbert space. *Proceedings of the National Academy of Sciences*, 17(5):315–318, 1931.
- [37] J. Kou and W. Zhang. An improved criterion to select dominant modes from dynamic mode decomposition. *European Journal of Mechanics-B/Fluids*, 62:109–129, 2017.
- [38] J. N. Kutz, S. L. Brunton, B. W. Brunton, and J. L. Proctor. *Dynamic Mode Decomposition: Data-Driven Modeling of Complex Systems*. SIAM, 2016.
- [39] J. N. Kutz, J. L. Proctor, and S. L. Brunton. Koopman theory for partial differential equations. *arXiv preprint arXiv:1607.07076*, 2016.
- [40] N. Kuznetsov. Stability of shock waves. *Physics-Uspeski*, 32(11):993–1012, 1989.
- [41] C. B. Laney. *Computational gasdynamics*. Cambridge University Press, 1998.
- [42] H. I. Lee and D. S. Stewart. Calculation of linear detonation instability: One-dimensional instability of plane detonation. *J. Fluid Mech.*, 212:103–132, 1990.
- [43] L. Massa, R. Kumar, and P. Ravindran. Dynamic mode decomposition analysis of detonation waves. *Physics of Fluids*, 24(6):066101, 2012.
- [44] I. Mezić. Analysis of fluid flows via spectral properties of the Koopman operator. *Annual Review of Fluid Mechanics*, 45:357–378, 2013.
- [45] S. Peitz and S. Klus. Koopman operator-based model reduction for switched-system control of PDEs. *arXiv preprint arXiv:1710.06759*, 2017.
- [46] L. Rezzolla. Stability of cosmological detonation fronts. *Physical Review D*, 54(2):1345, 1996.
- [47] F. Richecoeur, L. Hakim, A. Renaud, and L. Zimmer. DMD algorithms for experimental data processing in combustion, 2012.
- [48] C. W. Rowley and S. T. Dawson. Model reduction for flow analysis and control. *Annual Review of Fluid Mechanics*, 49:387–417, 2017.
- [49] C. W. Rowley, I. Mezić, S. Bagheri, P. Schlatter, and D. S. Henningson. Spectral analysis of nonlinear flows. *Journal of Fluid Mechanics*, 641:115–127, 2009.
- [50] P. J. Schmid. Dynamic mode decomposition of numerical and experimental data. *Journal of Fluid Mechanics*, 656:5–28, 2010.
- [51] P. J. Schmid. Application of the dynamic mode decomposition to experimental data. *Experiments in Fluids*, 50(4):1123–1130, 2011.
- [52] P. J. Schmid and D. S. Henningson. *Stability and transition in shear flows*, volume 142. Springer Science & Business Media, 2012.
- [53] P. J. Schmid, L. Li, M. P. Juniper, and O. Pust. Applications of the dynamic mode decomposition. *Theoretical and Computational Fluid Dynamics*, 25(1-4):249–259, 2011.
- [54] P. J. Schmid and J. L. Sesterhenn. Dynamic mode decomposition of numerical and experimental data. In *61st Annual Meeting of the APS Division of Fluid Dynamics*. American Physical Society, November 2008.
- [55] G. Sharpe. Linear stability of idealized detonations. *Proceedings of the Royal Society of London. Series A: Mathematical, Physical and Engineering Sciences*, 453(1967):2603, 1997.

- [56] G. Sharpe and S. Falle. One-dimensional nonlinear stability of pathological detonations. *Journal of Fluid Mechanics*, 414:339–366, 2000.
- [57] G. J. Sharpe. Linear stability of pathological detonations. *Journal of Fluid Mechanics*, 401:311–338, 1999.
- [58] M. Short and D. S. Stewart. Cellular detonation stability. Part 1. A normal-mode linear analysis. *Journal of Fluid Mechanics*, 368:229–262, 1998.
- [59] D. S. Stewart and A. R. Kasimov. Theory of detonation with an embedded sonic locus. *SIAM J. Appl. Maths.*, 66(2):384–407, 2005.
- [60] G. W. Swan and G. R. Fowles. Shock wave stability. *The Physics of Fluids*, 18(1):28–35, 1975.
- [61] S. I. Syrovatskii. The stability of shock waves in magnetohydrodynamics. *Soviet Phys. JETP*, 35:1024–1027, 1959.
- [62] K. Taira, S. L. Brunton, S. Dawson, C. W. Rowley, T. Colonius, B. J. McKeon, O. T. Schmidt, S. Gordeyev, V. Theofilis, and L. S. Ukeiley. Modal analysis of fluid flows: An overview. *arXiv preprint arXiv:1702.01453*, 2017.
- [63] B. D. Taylor, A. R. Kasimov, and D. S. Stewart. Mode selection in unstable two-dimensional detonations. *Combust. Theory Model*, 13(6):973–992, 2009.
- [64] J. H. Tu, C. W. Rowley, D. M. Luchtenburg, S. L. Brunton, and J. N. Kutz. On dynamic mode decomposition: theory and applications. *Journal of Computational Dynamics*, 1(2):391–421, 2014.
- [65] A. Tumin. Initial-value problem for small disturbances in an idealized one-dimensional detonation. *Physics of Fluids*, 19:106105, 2007.
- [66] J. von Neumann. Theory of detonation waves. Office of Scientific Research and Development, Report 549. Technical report, National Defense Research Committee Div. B, 1942.
- [67] M. O. Williams, I. G. Kevrekidis, and C. W. Rowley. A data-driven approximation of the Koopman operator: Extending dynamic mode decomposition. *Journal of Nonlinear Science*, 25(6):1307–1346, 2015.
- [68] A. Wynn, D. Pearson, B. Ganapathisubramani, and P. J. Goulart. Optimal mode decomposition for unsteady flows. *Journal of Fluid Mechanics*, 733:473–503, 2013.
- [69] Y. B. Zel’dovich. On the theory of propagation of detonation in gaseous systems. *J. Exp. Theor. Phys.*, 10(5):542–569, 1940.
- [70] H. Zhang, S. Dawson, C. W. Rowley, E. A. Deem, and L. N. Cattafesta. Evaluating the accuracy of the dynamic mode decomposition. *arXiv preprint arXiv:1710.00745*, 2017.
- [71] K. Zumbun. Stability of detonation profiles in the ZND limit. *Archive for rational mechanics and analysis*, 200(1):141–182, 2011.
- [72] K. Zumbun. Recent results on stability of planar detonations. In *Shocks, Singularities and Oscillations in Nonlinear Optics and Fluid Mechanics*, pages 273–308. Springer, 2017.